Microscopic Mechanisms for Skin Friction Reduction by Microbubbles

by

Yoshiaki Kodama, Kazuyasu Sugiyama[*1)]
Yuichi Murai[*2)] and Takafumi Kawamura[*3)]

Abstract

In order to clarify the skin friction reduction mechanism by microbubbles, both experiment and numerical simulation of turbulent channel flow with bubbles were carried out in the same parameter range, and were compared. In the experiment, silicone oil ten times more viscous than water has been used, in order to lower the Reynolds number to that of numerical simulation. The surface tension of the Silicone oil is 1/3 of that of water. In the numerical simulation, two numerical methods have been used. One is the Force Coupling Method (FCM), in which bubbles are assumed to be rigid and the influence of bubbles to the flow is simulated by body forces. The other is the Front-Tracking Method (FTM), in which fluid phase and gas phase are solved simultaneously and bubble shape is allowed to deform by being expressed with polynomials

In the experiment the Reynolds number (*Re*) is 2,777 to 4,500, and the Weber number (*We*) is 200. The experimental values of local skin friction shows that the flow is semi-laminar at *Re*=2,777 in the non-bubble condition, and that, by injecting bubbles, the skin friction increases to the turbulent flow value, which means that bubble injection stimulates the flow and turns it to fully turbulent. At Re=3,734(3,811) the flow is already fully turbulent in the non-bubble condition, and therefore adding bubbles has little influence on the flow, resulting in little change in the skin friction. At even higher Reynolds number of nearly 4,500, adding bubbles decreases skin friction slightly.

The Reynolds number of the numerical simulation using FTM is 3,000. The time history of skin friction shows that at the wall where bubbles are clustered by buoyancy local skin friction tends to show slight decrease by adding deformable bubbles (We=100). However, by adding less deformable bubbles (We=50) local skin friction slightly increases. Computation at We=200 has blown up. The local skin friction in the FCM computation at *Re*=4,000 shows 2.3% increase by adding (rigid) bubbles. Therefore it may be stated that, at *Re*=3,000, addition of deformable bubbles tends to decrease skin friction, while addition of less deformable bubbles, or rigid bubbles, tends to increase skin friction.

In order to carry out numerical simulation of turbulent shear flow with bubbles at higher Reynolds number, the simulation of the homogeneous turbulent shear flow (HTSF) with deformable bubbles has been carried out. The result shows that large turbulent Reynolds number, smaller shear Reynolds number and large Weber number have positive influence on the microbubble drag reduction. The increase of the turbulent Reynolds number of HTFS corresponds to the increase of the Reynolds number of the turbulent channel flow (TCF), and therefore the result agrees with the experimental result that added bubbles decrease skin friction at higher Reynolds number but not at lower Reynolds number. The Weber number dependence of the HTSF result can be compared directly with that of TCF. Thus the result confirms that bubble deformation acts to decrease skin friction.

*1) University of Twente, the Netherlands
*2) Hokkaido University
*3) The University of Tokyo

原稿受付　平成１８年１０月２５日
審 査 済　平成１９年１１月１９日

Table of contents

1. Introduction

Microbubbles, i.e. small air bubbles, injected into the turbulent boundary layer developing along a solid surface moving in water, have significant skin friction reduction effect with no harm to the environment, and are regarded as a promising drag reduction device for ships. For example, in 2001 there was a full-scale microbubble experiment using a training ship of length Lpp=120m running at 14 knots, a typical cruising speed of a large tanker, in which the drag of the ship reduced by as much as 5%. Although the drag reduction effect of microbubbles generated using existing techniques is large enough to be applied to slowly moving ships such as tankers, it is always desirable to have larger drag reduction per unit volume of injected air. In order to do so, it is first of all necessary to know the mechanism how skin friction decreases with bubble injection.

The skin friction reduction mechanism of microbubbles is not yet fully understood. One of the main reasons for the difficulty in clarifying the mechanism is the lack of confidence in direct numerical simulation (DNS) for this type of flow. At the time this project started in 2002, there was hardly any DNS result in which the skin friction reduction by microbubbles was successfully simulated, but in almost all the numerical simulations microbubbles increased skin friction. For example, see Kawamura and Kodama (2001 & 2002) and Sugiyama et al. (2002).

The only exception was that by Xu et al. (2002), in which they simulated the microbubble drag reduction using the Force Coupling Method (FCM). However, later, the accuracy of the result was found to be ambiguous, because Sugiyama et al. (2004) showed that, by increasing the accuracy of the computation by including not only the force monopole term, which was the case with Xu et al. (2002), but also the force dipole term, the simulation predicts skin friction increase.

In Kawamura and Kodama (2001 & 2002) the Front-Tracking (F-T) formulation generalized by Unverdi and Tryggvason (1992) was employed in order to resolve both liquid and gas phases with flexible bubble shapes. This computation was perhaps the most accurate for microbubble flows at that time, but, still, the skin friction reduction by microbubbles could not be simulated, and the skin friction increased with increasing void fraction.

The failure of DNS in simulating skin friction reduction by microbubbles posed serious questions to the validity of DNS for microbubble flows. This put a serious handicap to the study on the skin friction reduction mechanism, because DNS has successfully given numerous valuable information, which cannot be obtained experimentally, on complex flows such as turbulence.

Therefore we, the present investigators, proposed this research project to find out the reason for the discrepancy between experiment and numerical simulation, hoping to regain the validity of DNS. There are several conditions that are different between those of experiment and DNS. One is the bubble dispersion effect. In the experiment, bubbles that are injected from the wall are initially concentrated near the wall and are gradually dispersed away from the wall due to turbulence as they go downstream. This transient state was simulated by Sugiyama et al. (2003) using the Eulerian-Lagrangian (EL) method, and the skin friction reduction was obtained in the transient region.

Another different condition is the range of the Reynolds number. Although the channel flow is fully developed and turbulent in both experiment and DNS, the friction Reynolds number Re_τ of DNS is $O(10^2)$, one or two orders of magnitude smaller than that of experiment. We suspected that this was the main cause of the discrepancy and, since carrying out DNS at the same friction Reynolds number as that of experiment is impossible because of today's computer power, we decided to carry out experiment at the same friction Reynolds number as that of DNS, so that direct comparison of DNS and experiment becomes possible.

The second chapter describes the experimental work, in which silicone oil of 10 cSt viscosity, ten times more viscous than water, was used as fluid media. Water was also used in some experiments. The third chapter describes the DNS work, in which the flow conditions were made the same as those of the experiment as much as possible. The forth chapter describes numerical simulation of homogeneous shear flow with deformable bubbles. The Reynolds number and Weber number dependence of the bubble effect on the flow away from the wall is further studied. The fifth chapter describes discussions and conclusions.

2. Experimental Study of Microbubble Channel Flow

2.1 Outline of the study

The main purpose of the experimental study is to clarify the low Reynolds number behavior of bubbly channel flow. For that purpose, silicone oil was chosen as fluid media. Its physical property is shown in Table 2.1.

That is, the Silicone oil used in the experiment has approximately the same density as water, it is ten times more viscous than water, and it has surface tension less than 1/3 of water. Using this silicone oil, we can lower the Reynolds number to approximately 1/10 of that of water at the same flow speed. The smaller surface tension causes some difficulty in bubble generation, as described in later sections. Use of Silicone oil for low Reynolds number conditions provides a number of merits as follows: 1) Interfacial property of bubble surface is stable in comparison with water flow. Contamination effect is so negligible that the comparison with DNS can be discussed exactly. 2) The channel height is kept large at such a low Reynolds number condition because of high viscosity of oil used. This makes optical measurement easier, and the ratio of bubble diameter to channel height is adjustable to DNS as well. In addition to experiments using Silicone oil, normal experiments using water were also conducted for comparison.

The experimental devices constructed are as shown in Fig.2.1. For comparison with DNS's conditions, four kinds of horizontal straight channels have been made. A-Channel exists at Fukui University, and B-Channel at Hokkaido University. To vary the bubble diameter widely, i.e. 0.02 to 5.00 in the value of d/H, four types of bubble generation systems (porous plate method, capillary tube method, water electrolysis method, and laser-boring method) are employed. A1-Channel and B1-Channel were used in the water flow experiment, in which high Reynolds number channel flows (Re_H=5,000 to 20,000) are measured. The results using the B1 channel are omitted in this report. A2-Channel and B2-Channel, were used in the silicone oil flow experiment, in which low Reynolds number channel flows (Re_H=500 to 5000) are measured. The dimensions of the test section of each channel are shown in Table 2.2. Since the results using the B1-Channel are irrelevant to the present study, its dimensions are not shown in the table.

Fig.2.2 shows photographs of A-Channel and B-Channel.

Table 2.1 Comparison of physical properties of silicone oil and water

(at 20 deg. C)	Silicone oil	Water
density ρ (kg/m^3)	935	998
viscosity μ (kg/m.s)	10.38×10^{-3}	1.002×10^{-3}
kinematic viscosity ν (m^2/s)	11.10×10^{-6}	1.004×10^{-6}
surface tension σ (N/m)	0.0201	0.07275

Table 2.2 Dimensions of channel test sections

Channel	Fluid media	height H(mm)	half height h(mm)	width (mm)	length (mm)
A1	water	10	5	100	6,000
A2	silicone oil	10	5	100	6,000
B1	water	40	20	-	-
B2	silicone oil	20	10	160	6,000

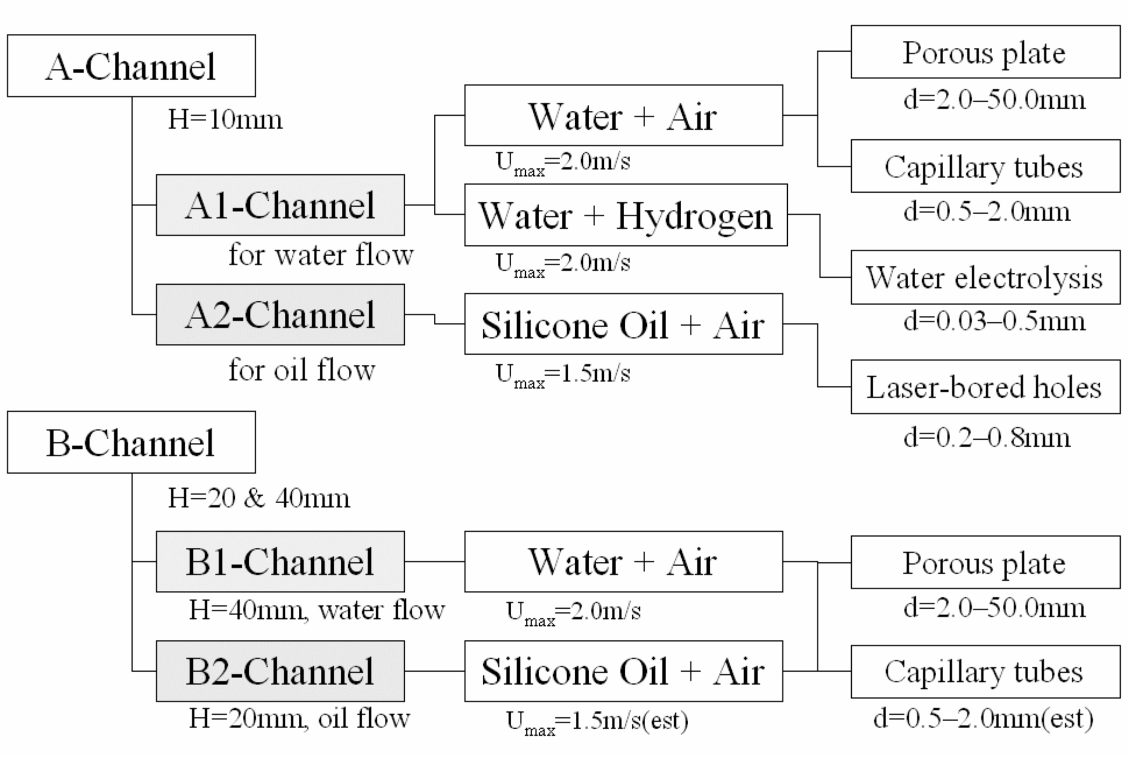

Fig.2.1 Experimental channels and the bubble generation devices

(a) A-Channel　　(b)B-Channel

Fig.2.2 Photographs of experimental channels

2.2 Water channel flow

2.2.1 Synchronized measurement of wall shear stress and large bubble behavior

(1) Purpose of study

The microbubble method, i.e. in which small bubbles are injected into the turbulent boundary layer, reduces the skin friction significantly. Takahashi *et al*. (2003) carried out experiments in the microbubble method using a long flat plate ship, and showed the drag reduction up to 22%. It is considered that the mechanism of this method is relevant to several factors, such as reduction of mean local density and effective viscosity or translational motions of bubbles and bubble deformation interacting with coherent structure of turbulence; however, the mechanism has not been clarified comprehensively. On the other hand, the air film method, i.e. in which relatively large bubbles are injected at the bottom of ships and they migrate over the surface, is also recognized as an effective drag reduction method. Katsui *et al*. (2003) carried out an experiment of the air film method using a tanker-form model ship. They showed that the skin friction drag reduction worked proportional to the area of air film. It implies that the drag reduction of the air film method is caused by preventing direct contact of the ship body with water. Both of the studies were carried out separately, and therefore the performance in the intermediate condition between microbubble and air film, i.e. a wide range of conditions of bubble diameter relative to the thickness of the boundary layer, has not been investigated explicitly. Moreover, owing to frequent coalescence and fragmentation of bubbles, the bubble diameter gradually changes and converges to an equilibrium size further downstream of the bubble injector. Therefore, it is important to study in such cases, in which the persistency of drag reduction effect will be discussed as well. In this part of study, direct measurement of time averaged skin friction is made in a horizontal channel in a boundary region between the microbubble and air film conditions for bubbles. In addition, the temporal relationship between local skin friction and bubble interfacial structure is investigated via the synchronized measurement, which will be described later in the section.

(2) Experimental method

The A1 channel is used in the experiment. A snapshot of the experimental apparatus is as shown in Fig.2.2. The test section is a horizontal rectangular channel made of transparent acrylic resin and is 10 mm in height, 100 mm in width and 6000 mm in length, respectively. Measurement windows locate in the upper wall of the channel at the interval of 250 mm in the streamwise direction. Tap water and room air are used for two phases at laboratory temperature (10 to 20 deg C). Air bubbles are injected into the horizontal channel through the air injection device, as shown in Fig.2.3. This device has a porous plate made of alumina with the nominal pore diameter of approximate 60 μm. The injection area is 14 x 48 mm^2. The bubbles are generated with compressed air supplied from outside the channel. The water circulates in the channel, and the bubbles are eliminated in the downstream region, by swirling the fluid in a bubble removable tank.

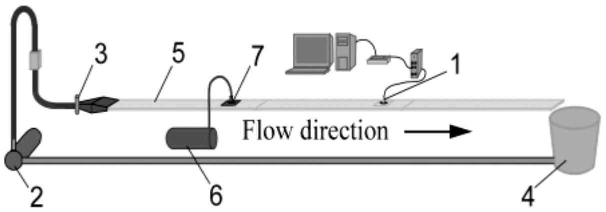

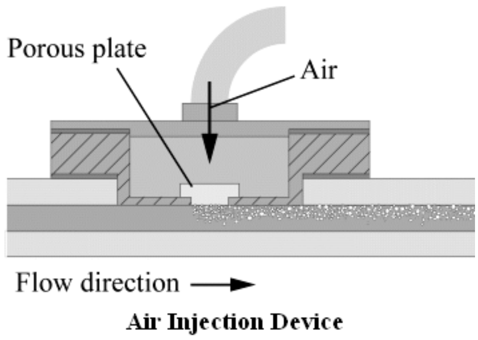

Fig.2.3 Experimental channel and air injection device (A1-channel)

The local wall-shear stress on the upper wall of the channel is measured by a shear transducer (SSK, S10W-01), which has the sensing part of 10 mm in diameter and the maximum load of 1 N, corresponding to 12.5 Pa of shear stress. A schematic diagram of the shear transducer is shown in Fig. 2.4(a) (b). In order to obtain the local wall-shear stress, the data are recorded to a PC through an amplifier and a data logger. The measurement of the shear stress is performed at x/h= 50, 200 and 800, which correspond to 250, 1000 and 4000 mm downstream of the air injection device.

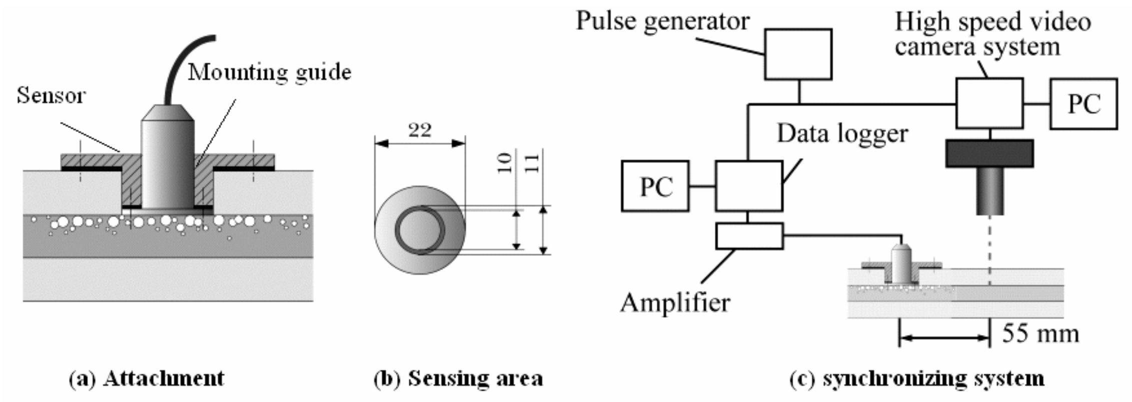

Fig.2.4 Attachment of shear transducer working with a high-speed video camera

The detail of the experimental conditions is listed in Table 2.3. The photography of interfacial structure of bubbles is recorded using a high-speed digital video camera (Photron, Fastcam-Max), on which a tele-centric lens is mounted. The back light projection is adopted by a metal halide lamp. The frame rate is 500 fps and the shutter speed is 1/150000 s. The image of gas-liquid interface can be obtained clearly by this illumination method. The images taken via the camera are recorded as digital raw data in a PC. The field of view is approximately 17.5 x 17.5 mm and the magnification factor is 0.00172 mm/pixel. Fig.2.4(c) shows a schematic diagram of the synchronized measurement system. A pulse generator synchronizes the trigger timings of the camera and the data logger. The image acquisition position is 55 mm downstream the measurement position of wall-shear stress, because they cannot be located at the same position. Hence there is a time lag between the data obtained by each device. The time lag is removed in the process of data correction using the mean velocity of gas-liquid interface, which is measured by particle image velocimetry (PIV).

Fig. 2.5 shows the result of wall shear stress obtained by the shear transducer in the case of single-phase water channel flow. The ordinate and abscissa stand for the local shear stress and bulk mean velocity in the channel, respectively. In this figure, there is a slight difference between the experimental and theoretical values. This discrepancy comes from a very small error for the flatness of the sensing area to the channel wall, and it is in the order of 10 micron estimated by a boundary layer theory. However the overall tendency in the both data takes similar, and there is only a relative error to Blasius's formula around –10% in the range tested, i.e. no significant random error. In practice, the ratio of two wall shear stresses for single- and bubbly flow cases can be evaluated with this method.

Table 2.3 Experimental conditions for water channel flow

Bulk mean velocity, U	1.0-2.0	[m/s]
Mean void fraction, α	0-26	[%]
$Re = UH/\nu, H = 2h$	12000-17000	[-]
$Re_\tau = U_\tau h/\nu$	340-610	[-]
$Fr = U(gh)^{1/2}$	4.5-9.0	[-]
$We = \rho_l U^2 h/\sigma$	70-285	[-]
Temperature of water	28	[deg.C]
Density of water, ρ	999	[kg/m^3]
Kinematic viscosity, ν	1.17×10^{-6}	[m^2/s]
Shear transducer :		
Sampling rate	1	[kHz]
Sampling time	60	[sec]

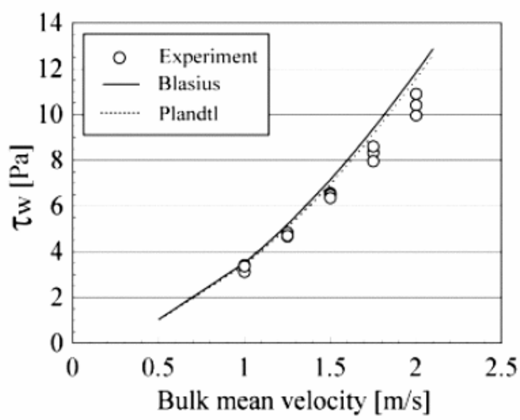

Fig.2.5 Wall shear stress without bubbles

(3) Experimental results

Fig. 2.6 shows the result of skin friction on the upper wall at *x/h*=50, 200 and 800, i.e. *x*=250, 1000 and 4000 mm downstream of the air injection device. The vertical axis shows skin friction coefficient ratio C_f / C_{f_0}, whose each component is defined as

$$C_{f_0} \equiv \frac{\tau_{w_0}}{\frac{1}{2}\rho_w U^2} \tag{2.1}$$

$$C_f \equiv \frac{\tau_w}{\frac{1}{2}(1-\alpha)\rho_w U'^2} \tag{2.2}$$

$U \equiv \frac{Q_w}{A_c}$; bulk flow speed in the non-bubble condition

$U' \equiv \frac{Q_w + Q_a}{A_c}$; bulk flow speed in the bubble condition, taking into account the air flow rate

ρ_w ; water density

Q_w ; water flow rate, which takes the same value in the non-bubble and bubble conditions

Q_a ;air flow rate

A_c ; channel sectional area

That is, corrections due to speed increase and density decrease are applied. It results that

$$\frac{C_f}{C_{f_0}} = \frac{1}{1-\alpha}\left(\frac{U}{U'}\right)^2 \frac{\tau_w}{\tau_{w_0}} \tag{2.3}$$

In the case of *x*/*h*=50 (see Fig. 2.6(a)), the skin friction ratio increases with increasing void fraction up to around 10 %. And then it begins to decrease at the higher void fraction. The skin friction ratio is lower than unity as the void fraction is given higher than 15 %. That is, the drag reduction occurs. The maximum drag reduction observed in the present experiment is approximately 40 % in all the conditions. It is also seen that the variation of the data owing to the speed of flow is obvious at the lower void fraction in the channel, and the skin friction ratio increases as the flow velocity decreases. To the contrary the deviation vanishes as the void fraction is given higher than 20 %. By paying attention to the difference in measurement points, the skin friction ratio always lower than unity for the case of *x*/*h*=200 and 800 (see Figs. 2.6 (b) and (c)). And the skin friction decreases approximately linearly for the high void fraction. This fact implies that there is a transient effect of two-phase boundary layer developing in the streamwise direction on the wall shear stress. The distance of transient effect depends on the speed of channel flow. On the other hand, the two-phase boundary attains to an equilibrium state in the downstream region, which is nearly independent on the speed of flow. When the void fraction is higher than 20 %, it is confirmed that the skin friction ratio approaches a certain value in any flow velocities and measurement positions.

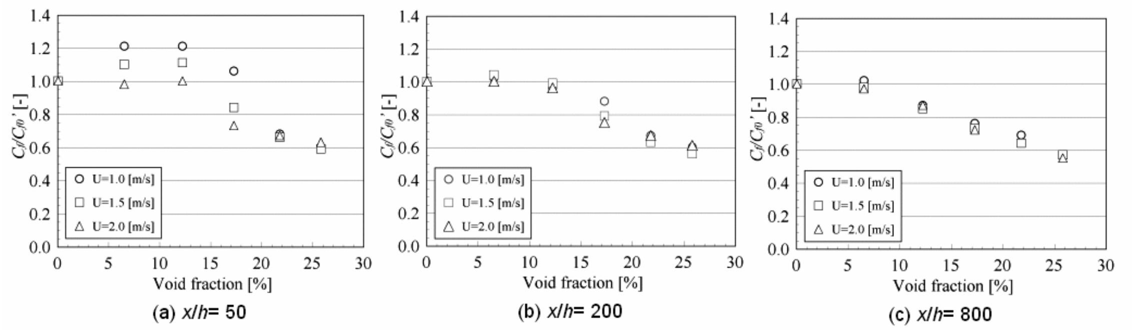

Fig.2.6 Friction coefficient ratio at three locations as function of void fraction

The gain factor of skin friction reduction to void fraction is shown in Fig. 2.7(a). The gain factor indicates the magnitude of the drag reduction effect per void fraction. In this figure, it is observed that the gain increases with increasing void-fraction in all the conditions tested, and reaches up to approximately 1.6 when the void fraction is higher than 20 %. In this experiment, the range of the gain is scattered from –3.0 to 1.6, and its absolute value exceeds unity. That means the drag modification caused in this channel is not originated by simple mechanism such as a mean density decrease. Thus, bubbles in the case of low void fraction and low flow speed generate additional skin friction more than its volume fraction, and bubbles in a high void fraction reduce the friction more than its volume fraction. This tells us that a structural alternation happens inside the boundary layer as bubbles are mixed. Fig.2.7(b) shows the relationship between mean bubble diameter and bulk mean void fraction. In this figure, it is confirmed that the bubble diameter becomes larger with increasing bulk mean void fraction and distance from the bubble injection device.

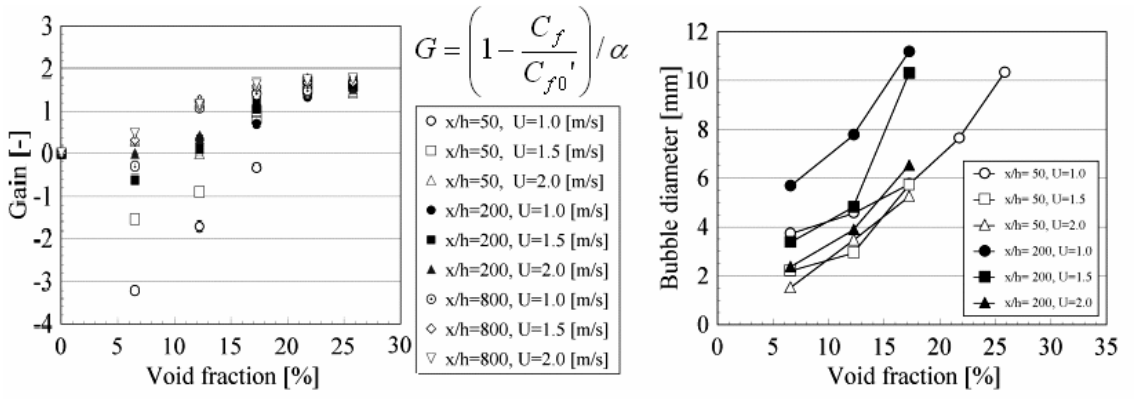

(a) Gain defined by the above formula　　(b) Bubble diameter averaged

Fig.2.7 Gain of drag modification and bubble diameter as function of void fraction

Fig. 2.8(a)(b) shows the temporal correlation of the skin friction ratio to the local projection void fraction β for 1.0 m/s of the bulk mean velocity and 20% of bulk mean void fraction in channel, where the measurement positions are x/h=50 and 200 downstream of the air injection device. In those cases, approximately 30% of the drag reduction is obtained as the time averaged value. Fig. 2.8(c) explains the local projection void fraction β, which is defined as the ratio of the white area i.e. the projected bubble area, in the right half of Fig.2.8(c).

In Fig. 2.8(a)(b), the ordinate stand for the ratio of wall-shear stress (denoted by the heavy line) and the local projection void fraction (denoted by the thin line), respectively, and the abscissa stands for the time. When the projection void fraction is unity, it is that only air bubbles cover over the sensing part of the shear transducer. On the contrary, when the void fraction becomes 0, it indicates that only liquid exists at the sensing part. The images on the upper part are the time expansion image taken via the synchronized measurement. Fig. 2.8(d) shows an element of time expansion image. The direction of the flow is from right to left in the time expansion images. In total, it is clear that there is a negative correlation between the local skin friction and the local void fraction. And it can be seen that the local skin friction decreases especially in the rear part of large bubbles, and increases after the bubbles pass through the measurement part. When the size of bubbles becomes larger (in other words, β takes unity for a long time), the skin friction decreases continuously for a long time. While the β takes 0, the ratio of wall-shear stress is the same as the case of single-phase water flow. These results are observed typically in the case of downstream positions because the bubbles become larger and migrate periodically on the downstream position than on the upstream one. Here, we discuss the local skin friction profile along each bubble by analysing the data set of the synchronized measurement.

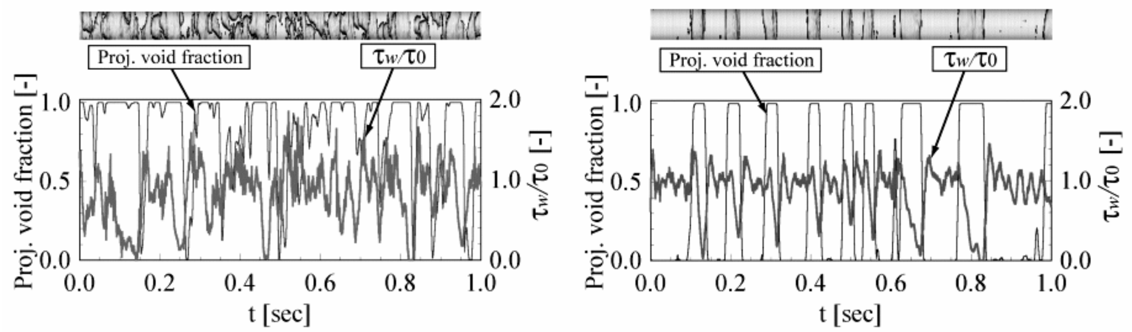

(a) U= 1.0 m/s, α= 20 %, x/h = 50 (b) U= 1.0 m/s, α= 20 %, x/h = 200

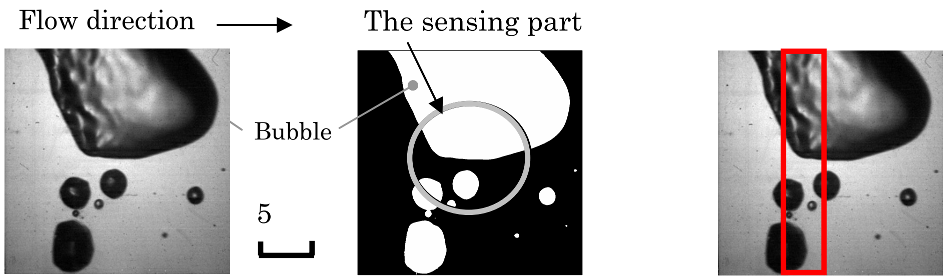

(c) Definition of local projection void fraction β (d)An element of time expansion image

Fig.2.8 Synchronized measurement of local skin friction and local projection void fraction

Fig. 2.9(a) shows the relationship between the local skin friction and dimensionless bubble coordinate in the streamwise direction, where the streamwise bubble length ranges from 20 to 70 mm. Here, the dimensionless bubble coordinate is defined as the ratio of the distance from the front of bubbles (t) to the total length of a single bubble (T). The dimensionless bubble coordinate of unity corresponds to the rear edge of bubbles. With this figure, it is found that the skin friction increases in the front part but decreases at the middle part, and then takes the minimum value at the rear part of the bubbles. The deviation of the skin friction from unity is larger in the latter half of the bubble more than in the former half, being providing drag reduction in total. These tendencies are confirmed similarly for bubbles of different size.

Fig. 2.9(b) shows the relationship between the mean skin friction inside single bubble and the streamwise bubble length. Fig. 2.9(c) shows the relationship between the bubble length and the least friction in a single bubble. The ordinate in these two figures is normalized by the single-phase wall-shear stress. In these figures, drag reduction always occurs during the bubble passage through the measurement point. Also, the skin friction decreases with increasing bubble length. In Fig. 2.9(c), when the bubble length takes a higher value than 50 mm (5 H or 10h), the skin friction takes nearly 0 during the passage of the bubble. This is a sort of locally segmented air film, which has a shear-free structure inside itself. The critical bubble length at which the shear-free structure takes place (50mm in this study) might be a new target of the investigation.

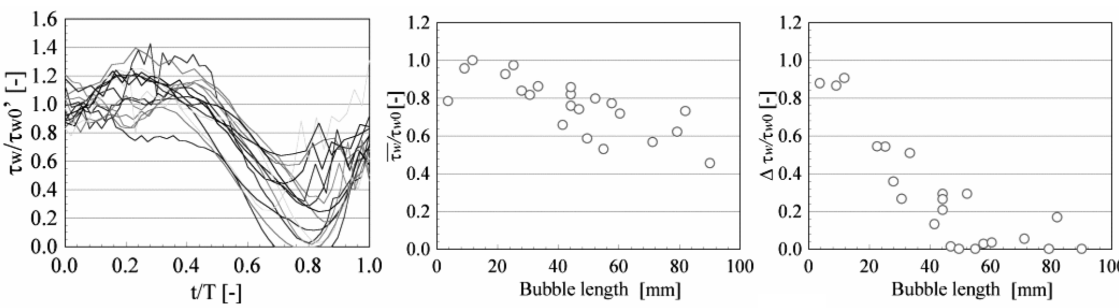

(a) Local friction inside bubble **(b) Average friction v.s. bubble length** **(c) Least friction v.s. bubble length**

Fig.2.9 Ensemble statistics of skin friction for individual bubble

Summarizing the measurement results, the following points have been made clear.

(i) The skin friction ratio initially increases with increasing void fraction, and then begins to decrease at the higher void fraction. In this process, the gain factor(drag modification ratio to void fraction) is more than unity in the absolute value, implying sensitive control of the skin friction by bubbles.

(ii) There is a clear negative correlation between the local skin friction and the local void fraction. Especially, the friction decreases drastically in the rear part of individual bubble.

(iii) The mean skin friction takes a maximum value in the case of bubbles around 10mm (1.0*H*) injected. The smaller and the larger size than it enhances drag reduction.

(iv) The local average skin friction inside individual bubble decreases with increase of bubble's streamwise length. In the case of bubbles larger than 50mm (a critical size, *d/H*=5), the local skin friction becomes zero.

2.2.2 Velocity measurement using Particle Tracking Velocimetry

(1) Purpose of study

Most of former experimental studies were implemented to evaluate Reynolds stress profile only in liquid phase, and did not consider explicitly the turbulent shear stress as two-phase flow, which is a function of local bubble motion as reported by Kataoka and Serizawa (1989, 1990). In this part of study, the momentum conservation equation of gas-liquid two-phase flow is used to acquire the componential turbulent shear stress as two-phase flow from experimental data obtained by Particle Tracking Velocimetry (PTV).

(2) Experimental method

A schematic diagram of the experimental apparatus is shown in Fig. 2.10(a). The configuration of the channel is the same as the one mentioned in Section 2.2.1, i.e. the A1 channel was used. The measurement location for PTV is at 250mm from the bubble injector device. The image acquisition of the two-phase flow is carried out using a high-speed digital video camera (Photron, Fastcam-Max-120KC, 512x512pixels) with a tele-centric lens (Computar, TEC-55). Fig. 2.10(b) shows the flow visualization system for PTV measurement. The tracer particles with 40 micrometer in average diameter are seeded to visualize the liquid phase flow. A metal halide light is used for illuminating the particles from the backside of the camera. In the present study, the backlight projection is implemented in the spanwise direction and the focal plane is adjusted on the central plane of the channel. The narrow depth of field is utilized to perform two-dimensional measurement of the flow. The frame rate is 4000fps and the shutter speed is 1/150000s. The image of gas-liquid interface is clearly obtained as well via this illumination method. The images taken by the camera are recorded as digital raw image data in a PC. The field of view is approximately 12x12mm and the magnification factor is 0.00225mm/pixel.

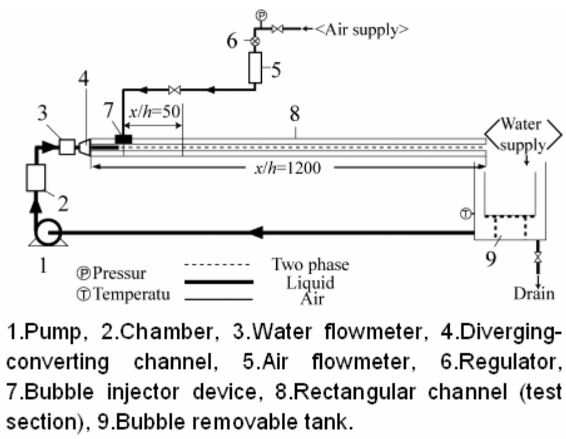

(a) Experimental channel for PTV

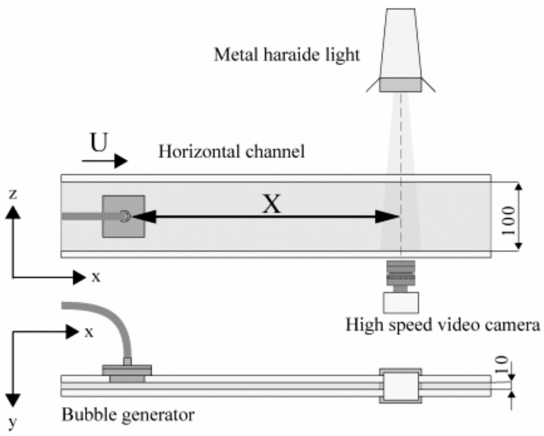

(b) Measurement section

Fig.2.10. Experimental set-up for particle tracking velocimetry

Fig. 2.11(a) shows a sample of the original image obtained by the above-mentioned photographing method. The size of the photograph is 12mm horizontally and 10mm vertically, equalling the channel height. Both blunt particles and clearly focused particles exist in the image for the intentionally narrowed depth of field. The degree of the focusing of lens can be evaluated by converting the image to spatial frequency spectrum. Focused particles have a high frequency band while defocused particles have a relatively low frequency band in the spectrum-base image. Thus, the focused particles can be extracted using a high-pass filter for the image as shown in Fig. 2.11(b). In contrast, blunt defocused bubbles and unclear particles existing outside the depth of field are removed with the high-pass filtering. Very small dark spots in the figure are the tracer particles. Individual bubble motion is measured by calculating the centroid of each bubble after image processing consisting of binarization and median filtering as shown in Fig.2.11(c). Local projection void fraction β is measured using another set of bubble images as shown in Fig.2.11(d), in which those bubbles contacting the top wall, being removed in Fig.2.11(c), are maintained.

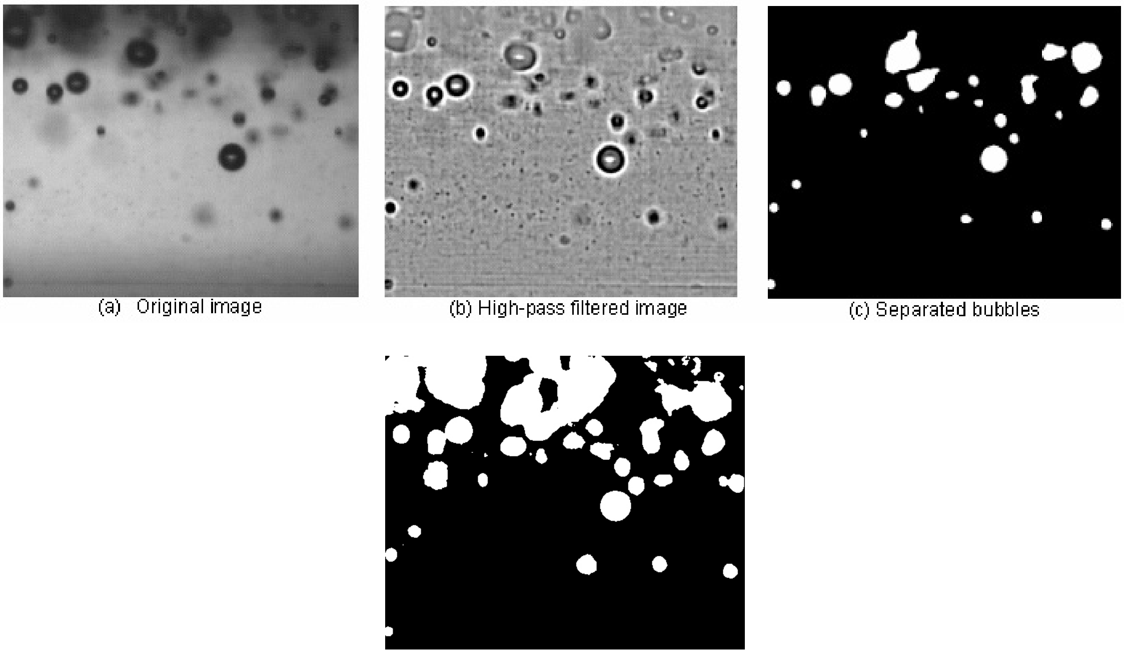

(d)Separated bubbles (for projection void fraction β)

Fig.2.11 Bubble and particle images for particle tracking velocimetry (x/h=50, U=2.0m/s, α=0.08%)

(3) Experimental results

Fig. 2.12(a) shows the mean void fraction profile across the channel height. The domain size defined here is 0.11mmx0.11mm. In this figure, y/h=0 is the upper wall and y/h=2.0 the lower wall. The local void fraction takes the highest value at y/h=0.2, while it is nearly 0 in the lower half region of the channel.

Fig. 2.12(b) shows the mean velocity profiles of liquid and bubbles in the top half coordinate of the channel, which is normalized by u_{max}. Here, u_{max} is the maximum velocity of liquid phase at the center of the channel. The liquid phase velocity follows the $1/7^{th}$ power law approximately at x/h=50 from the bubble injector device. The bubble velocity profile has a slightly slower velocity than the liquid-phase. Integration of the projected void fraction across the channel by assuming uniform spanwise distribution gives bulk void fraction 1.92%, which is 24 times the actual bulk void fraction α=0.08%.

Fig.2.12(c) shows the histogram of bubble diameter obtained by image processing. The mean bubble diameter is 0.7mm.

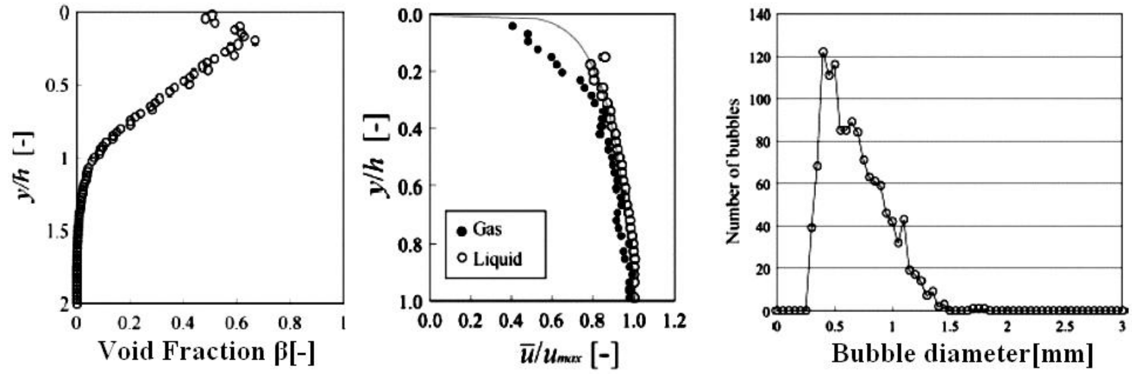

(a)Projected local void fraction β　　(b) velocity　　(c) bubble diameter

Fig.2.12 Time averaged profiles at measurement section (x/h=50, U =2.0m/s, α =0.08%)

Eq.(2.4) is derived from the momentum conservation equation of a bubbly two-phase mixture using a Reynolds average technique. In the two-phase flow, the turbulent shear stress consists of four terms as bellow,

$$\tau = \mu \frac{\partial \bar{u}}{\partial y} - \rho\left(1-\bar{\alpha}\right)\overline{u'v'} + \rho\bar{u}\overline{\alpha'v'} + \rho\overline{\alpha'u'v'} \quad (2.4)$$

where ρ and μ are the density and the viscosity of liquid phase. α, u and v are local void fraction and instantaneous velocity components in the streamwise and the vertical directions. In Eq.(2.4), the first term of the right-hand-side is viscous shear stress, which is dominant only near the wall surface. The second term is known as Reynolds shear stress, of which absolute value is always reduced by mixing bubbles because of the factor (1-α). The third and fourth terms are added components as two-phase correlation. The third term takes a value if the local fluctuations of void fraction α' and the wall perpendicular velocity component of liquid have a correlation. The fourth term is significant as two-velocity components u', v', and local fluctuation of void fraction have a correlation.

Fig.2.13(a) is the Reynolds shear stress profiles of single-phase channel flow. The stress is normalized by u_{max}^2. It is worth noting that the near-wall region of the channel cannot be exactly measured owing to the optical restriction for PTV. The near-wall region should be measured using an alternative technique in the future – some trials have been performed already but the data are still in discussion.

Fig.2.13(b) shows the componential profiles of turbulent shear stress divided into three terms. The measurement results have shown that the vertical correlation α'v' denoted by green triangular markers had a negative stress in the top half of the channel contributing to the drag reduction though the triple correlation α'u'v' denoted by blue diamond markers had a small positive stress. These results suggest that there is a certain organized interaction between two phases in the bubbly layer of the channel. In particular, we need to investigate what produces significant negative value for the vertical correlation to elucidate the mechanism of the drag reduction at this range of bubble size. Fig.2.13(c) shows the similar measurement results obtained by a larger domain size (four times) for the volume averaging than the previous case. The results confirm that the two-phase correlation terms have smaller value because of enforced averaging. With this confirmation, it is further estimated that the spatial scale of the elementary event that produces the two-phase turbulent correlation is smaller than the domain size adopted here. In other words, the drag-reducing event happens in the order of bubble size in the spatial scale, and is dominated by individual bubble motion in the turbulent shear layer.

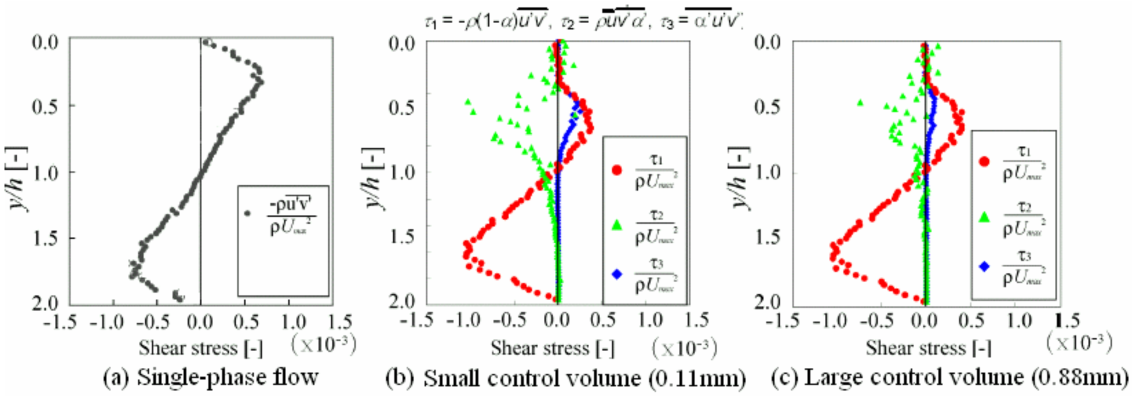

Fig.2.13 Turbulent shear stress profiles at x/h=50

The mechanism of producing a negative value for the vertical correlation stress is considered to relate to the individual bubble behavior. With this idea we have carried out high-speed video recording to observe bubbles' motion in the vicinity of the upper wall. Fig.2.14 shows consecutive pictures of bubbles in the vicinity of the top wall surface. Fig.2.14(a) shows the case of focusing a rising bubble as marked by a red circle. This bubble has vertical rise velocity of around 10% of streamwise velocity, and deforms as it displaces in the vertical direction because of sudden change in the velocity gradient. The diameter of this bubble was approximately 0.6mm. This bubble starts displacing downward after reaching the nearest point to the wall surface. Consequently this bubble oscillates in the vertical direction and produces vertical velocity fluctuation of the liquid phase around the bubble.On the other hand, we see frequently other type of vertical oscillation for small bubbles, which has much shorter typical wavelength of the oscillation than the case of large bubbles. Fig.2.14(b) shows the case of a dropping bubble. A possible cause of this type of oscillation is organized turbulent structure such as streamwise vortices and bursting phenomenon in the vicinity of wall. In fact, this type of bubble motion is observed irregularly. We think that there are four factors contributing to the vertically oscillating motion of bubbles; i.e., i) streamwise slip velocity between two phases, ii) buoyancy of bubbles, iii) bubble-bubble interaction and iv) large-scale turbulence structure. Owing to the streamwise slip velocity and buoyancy, a bubble, which reached up near the wall, receives a strong lift force and is pushed back downward. The balance among added inertia, lift, and buoyancy acting on individual bubble induces the oscillation. Owing to the turbulent structure, the vertically oscillating motion of bubbles irregularly occurred similar to sweep and ejection phenomena.

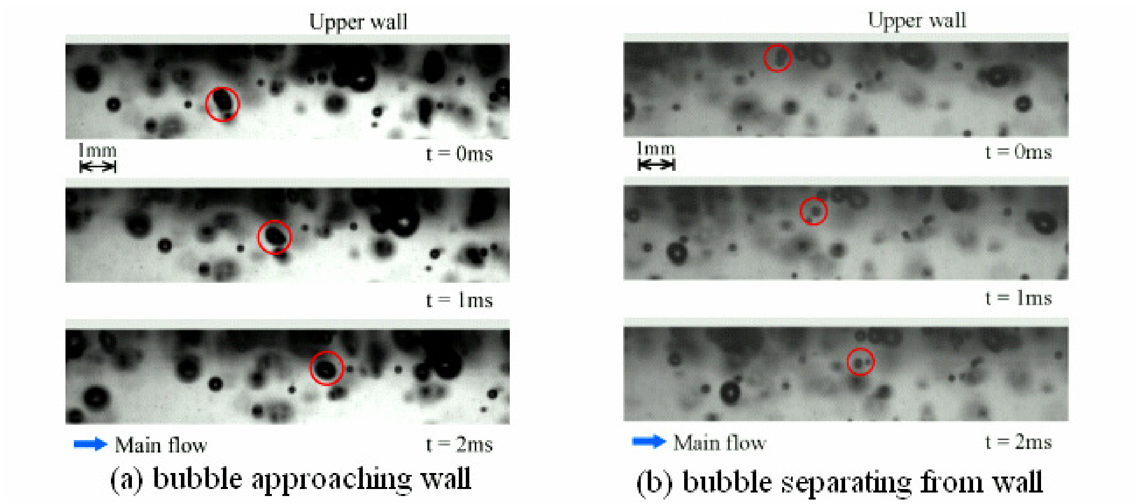

Fig.2.14 Bubble's oscillatory motion perpendicular to wall

Summarizing the measurement results, the following points have been made clear.

(i) The correlation $\alpha' v'$ produces a significant negative shear stress in the upper half of the channel, which contributes to the drag reduction. On the other hand, the triple correlation $\alpha' u' v'$ has a small positive stress.

(ii) A vertically oscillating motion of individual bubble is observed frequently in the vicinity of top wall surface, which is probably a major factor to produce the negative turbulent shear stress $\alpha' v'$.

2.3 Silicone oil channel flow

2.3.1 Bubble generation in Silicone oil channel flow

(1) Purpose of study

Silicone oil and air are used to realize a low Reynolds number channel flow to correspond with the simulation condition of DNS. Usage of silicone oil ensures stable property of the gas-liquid interface as well. Before implementing the measurement, the bubble generation characteristics in silicone oil medium is examined, which is estimated quite different from the case of water.

(2) Experimental results

The A2 channel was used in the bubble generation experiment. Fig.2.15(a)(b) show the difference of bubble generation between water and Silicone oil as liquid. The mean liquid velocity is 1.5m/s in all the cases. Using conventional capillary tubes having been used for water experiments, a long steady cavity is formed behind individual tube in the case of Silicone oil because of high viscosity (see picture (b)). Therefore, we made a bubble-generation plate on which two lines of very small holes of 50 micrometer in internal diameter are provided using laser-boring technique. Using this plate small and uniform bubbles less than 1mm in diameter are stably generated as shown in Fig.2.15(c). There are three factors for this success, 1) bubbles are broken easily by the shear stress of liquid because of low surface tension, 2) shear force itself is strong in case of high viscosity, 3) there is no coalescence once the bubbles are generated since the bubble surface is stable, i.e. the surface does not involves contamination in case of this oil.

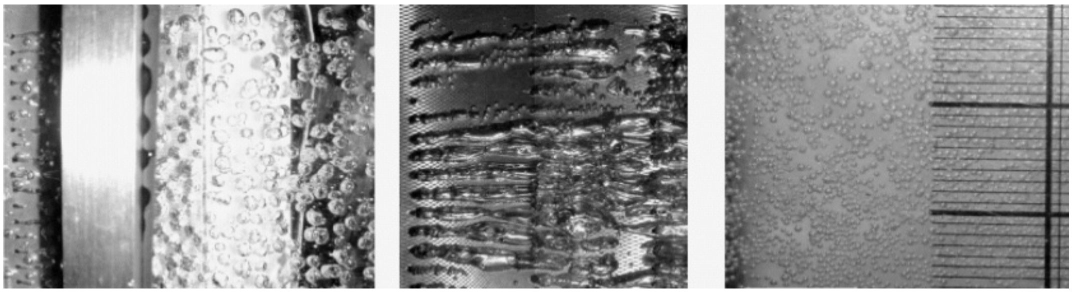

(a) Water/ID=1mm　(b)Si.Oil/ID=1mm　(c)Si.Oil/ID=0.05mm

Fig.2.15 Pictures of bubbles in silicone oil channel flow at 1.5m/s

Fig.2.16 shows the histogram of the bubble diameter in Silicone oil flow at U=1.5m/s. The bubbles are generated using laser-bored 0.05mm inner diameter holes. The bubble diameter is measured by image processing. Three different cases in the bulk void fraction are tested as shown by “%” in the figures. The diameter mainly distributes in the range of 0.2 – 0.8mm, and there is no significant difference between the upstream and the downstream sections. This result indicates that the bubbles once generated do not show coalescence and fragmentation in the downstream region.

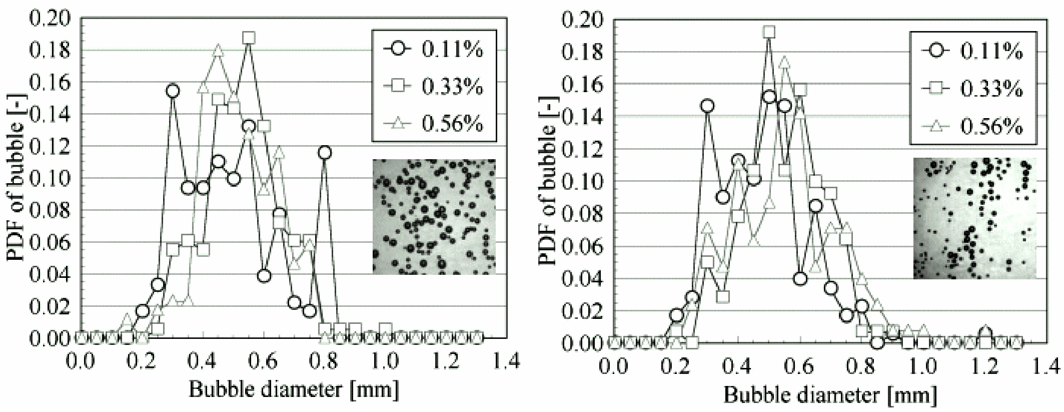

(a) x/h=50 (b) x/h=200

Fig.2.16 Bubble diameter in silicone oil channel flow at U=1.5m/s (ID=0.05mm)

Fig.2.17 shows the histogram of the bubble diameter at U=0.5m/s. The bubbles are generated using 0.1mm inner diameter needles shown in Fig.2.20. The mean void fraction in the channel increases up to 2.0%. If it is compared with Fig.2.16, the average bubble diameter increases as well as the peak diameter, and those are 2.0mm and 1.5mm, respectively. There is no significant difference between the results in two locations.

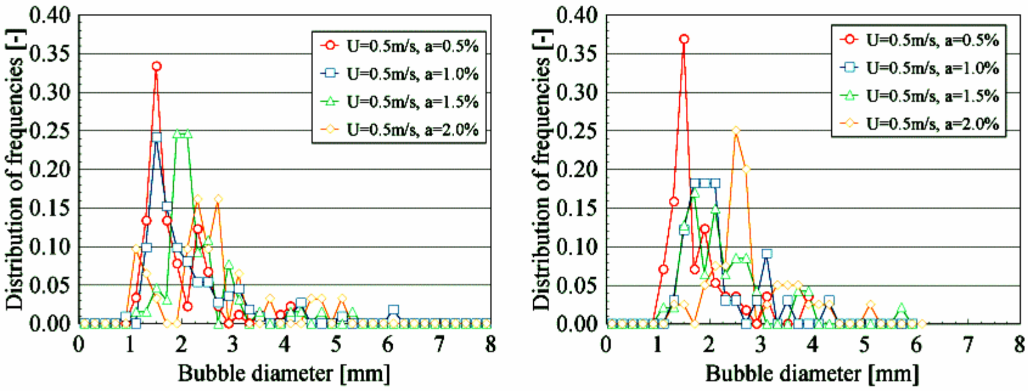

(a) x/h=50 (b) x/h=200

Fig.2.17 Bubble diameter in silicone oil channel flow at U=0.5m/s (ID=0.1mm needle)

2.3.2 Drag modification in laminar flow

(1) Purpose of study

As a basic study of drag modification, laminar channel flows are tested using Silicone oil. It is expected that the frictional drag increases with presence of bubbles due to additional friction produced by bubbles near the wall. The measurement in this condition is carried out to confirm the theoretical estimation in low Reynolds number channel flows.

(2) Experimental method

The channel used is the A2 channel of 10mm (h=5mm) height, 100mm width, and 6000mm length. Silicone oil of 8 to 10cSt in kinematic viscosity, 930 to 945kg/m^3 in density, circulates in all the loop of the facility via a positive displacement type pump. Floating cell type of oil flow meter is used to measure the liquid flow rate. The shear transducer (SSK, S10W-02) of which maximum load is 0.2gf per 10mm in sensing area diameter is used to measure the wall friction. This shear transducer is originally made for water flow measurement, however it works successfully for the Silicone oil as well if the relative value is measured. The data recorder (Keyence, NR2000) is used to import the signal of the transducer into PC. The sampling interval is 1ms (1kHz). The sampling period is chosen 60s, which is sufficiently long as the dimensionless time of the present channel flow (3000 dimensionless time).

The liquid temperature increases slowly during the experimental operation due to high viscosity and significant energy loss inside a couple of valves, a streamer and a flowmeter. The temperature is measured in every experimental condition, and it ranges from 23 to 37 degree C. The measurement section locates at 250mm (x/h=50) and 1000mm (x/h=200) from the bubble injection device. The void fraction varies from 0 to 2.0%. Laboratory room temperature is 17 degree C. For the photographing and bubble velocity measurement, a high-speed camera (Photron Fastcam-Max) is mounted on the channel. The frame rate is 1000fps, and electronic exposure time is 10^{-6}s. F-number of the lens is 5.6. Table 2.4 shows the details of the experimental conditions. Three kinds of mean liquid velocity, and four steps of void fraction are chosen as the experimental parameters.

Table 2.4 Experimental conditions (Laminar flow)

Bulk mean velocity of oil, U [m/s]	0.5	1.0	1.5
Bulk mean void fraction: α [%]	0, 0.5, 1.0, 2.0	0, 0.5, 1.0, 2.0	0, 0.5, 1.0, 2.0
$Re: UH/\nu,\quad H=2h$	538	1077	1615
$Fr:\ U(g\ \ h)^{-1/2}$	2.25	4.52	6.78

(3) Experimental results

Fig.2.18(a) shows the measurement results of friction coefficient ratio in silicone oil channel flow. In general, the friction coefficient increases after bubbles are mixed at any conditions. The typical gain factor ranges from 2 to 20 (i.e. in the order of 10). The drag increase is, however, not the monotonic function of the mean liquid velocity. In the upstream measurement section x/h=50, the drag increases at U=0.5m/s, and further increases at U=1.0m/s, but then decreases at U=1.5m/s. The increment ratio of the friction coefficient at Re=1615(U=1.5m.s) is around +2%.

The bubble shapes photographed from the top of the channel in four conditions are shown in Fig.2.18(b). The bubbles are almost spherical at U=0.5m/s in both two locations but elongated significantly in the streamwise direction at U=1.5m/s.

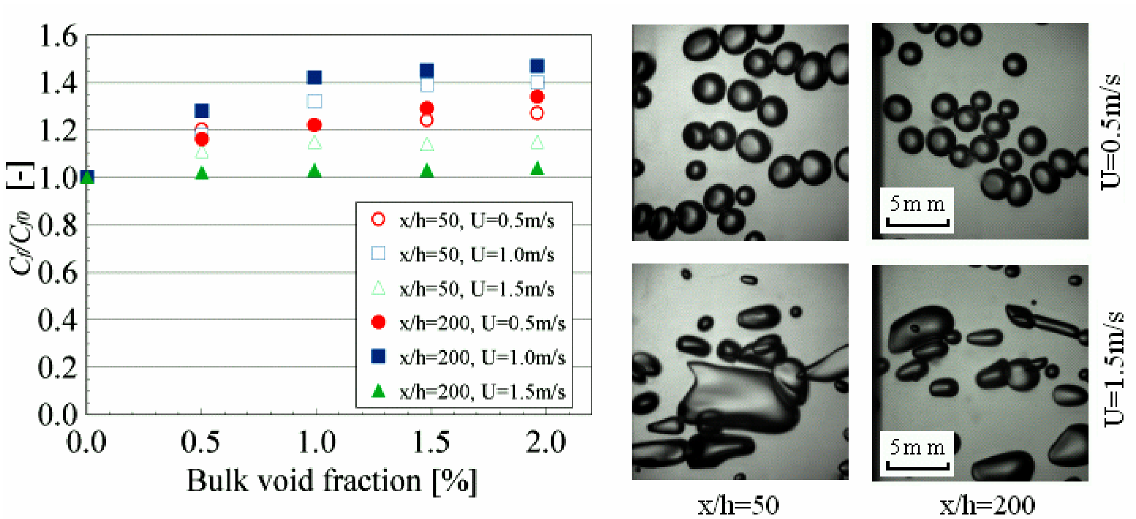

(a) friction coefficient ratio　　(b) bubbles /top view

Fig.2.18 Friction coefficient ratio and bubble's figure

Fig.2.19 shows probability density distribution of bubble's streamwise velocity at two locations. The bubble velocity is measured by particle tracking velocimetry applied to the individual bubble image. It is confirmed with this result that the average velocity of bubble is significantly slower than the liquid velocity. It is around a half of the mean liquid velocity. This implies that many bubbles in the channel accumulate in the vicinity of the channel wall. Assuming a parabolic profile in laminar liquid flow velocity, the bubble position on which liquid has a half of mean velocity is calculated as y/h=0.18 from the wall surface. The measurement results also indicate that the peak bubble velocity increases at high void fraction. Considering the result of friction coefficient with this result, it is suspected that the presence of many bubbles in the vicinity of the channel wall increases the local liquid velocity and thus increases the shear rate near the wall. The increased liquid velocity transports bubbles in such a case.

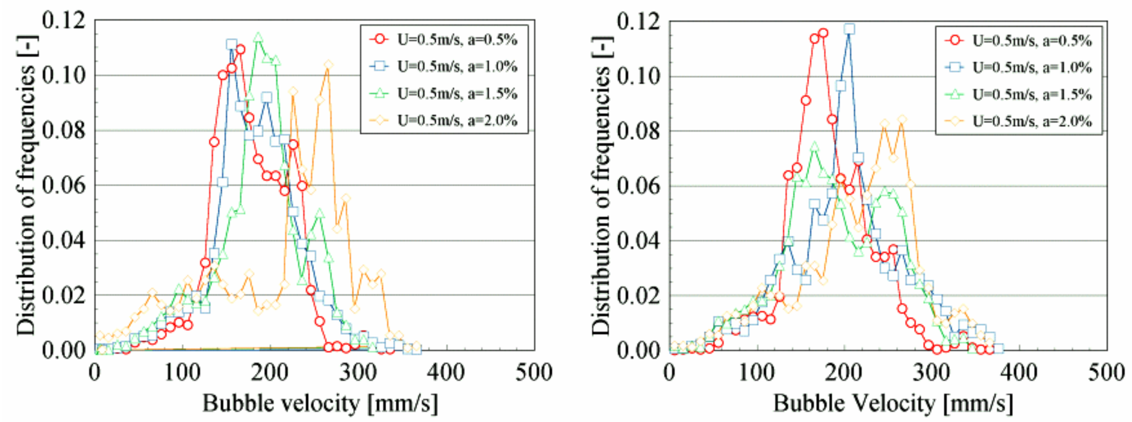

(a) x/h=50 (b) x/h=200

Fig.2.19 Probability density distribution of bubble velocity obtained by PTV

2.3.3 Drag modification in laminar-to-turbulent transitional flow

(1) Purpose of study

In the laminar-to-turbulent transition region of the channel flow, it is expected that the frictional coefficient suddenly rises as Reynolds number increases because of the transition. In such a sensitive region, it is important to know how bubbles affect the transition as well as to confirm the possibility of the drag reduction in the post-transition states. In addition, this experiment employs a larger channel height in comparison with the former case so that similarity of the drag modification can be discussed.

(2) Experimental method

The channel used is the B2 channel of height H=20mm (h=10mm), 160mm width, and 6000mm length. Silicone oil of 10cSt in kinematic viscosity, 935kg/m^3 in density, circulates in all the loop of the facility via a centrifugal pump. Floating cell type of oil flow meter is used to measure the liquid flow rate. Bubbles are injected through 140 stainless capillary needles that are arranged in three lines as shown in Fig.2.20(a). The needles, each having 0.1mm inner diameter and 0.3mm outer diameter, are arranged with 3mm spanwise and 10mm streamwise pitches, and 2mm protrusion from the wall. The bubble injection device locates at 300mm downstream of the inlet part of the channel. Bubbles are generally accumulating near the upper wall and provide non-uniform distribution as shown in Fig.2.20(b). The shear transducer (SSK, S10W-04) of which maximum load is 0.4gf per 10mm in sensing area diameter is used to measure the wall friction. A data recorder (Keyence, NR2000) is used to import the signal of the transducer into PC. The sampling interval is 1ms (1kHz). The sampling period is chosen 30s, which is sufficiently long as the dimensionless time of the present channel flow (1500 dimensionless time). The liquid temperature is kept constant at 21 degree C. The measurement sections are located at 300mm (x/h=30) and 900mm (x/h=90) from the bubble injection device. The void fraction varies from 0 to 2.5%. For the photographing of bubbles, a digital camera (Nikon, Coolpix 4500, 4.0Mpix) is used.

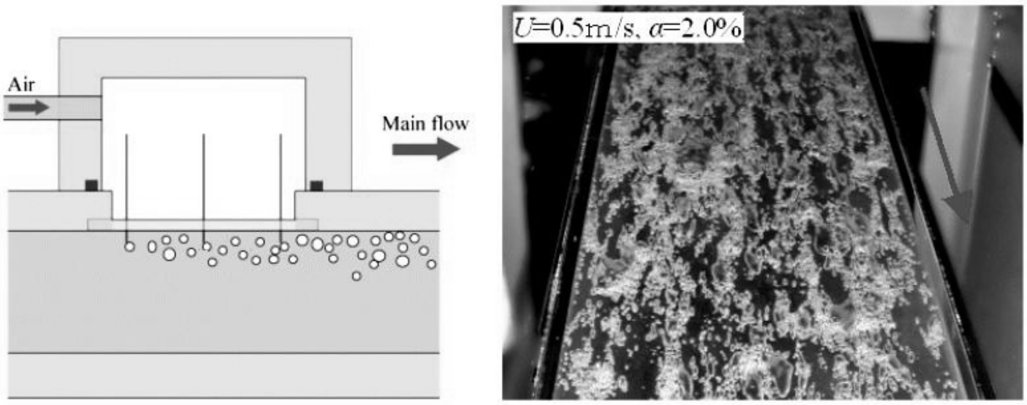

(a) Capillary needles for bubble injection　　(b) Top view of bubbles in the channel

Fig.2.20 Bubble injection device and overview of bubble flows in the channel

Tables 2.5 and 2.6 show the details of the experimental conditions. Four values of mean liquid velocity, and six steps of void fraction are chosen as the experimental parameters. The bubble diameter is set around 1mm but varies with the liquid velocity and the void fraction. The bubble diameter is measured by image processing for non-overlapping bubbles in the image. The kinematic viscosity and the surface tension are set as shown in the table so that Weber number *We* ranges from 10 to 230. With this condition, the bubbles have significant deformation due to the shear stress in the boundary layer, thereby the role of the bubble deformation takes place though the flow is low Reynolds number turbulent flow.

A tripwire is used to enhance the turbulent flow transition and ensure the reproducibility of the measurement since the transition region is targeted here. The trip wire has a screw form consisting of two thin stainless steel fibers. It is 0.5mm in diameter and 400mm in total length. The wire is located upstream the bubble generator at x/h= - 50 (x= - 500mm). The wire is set such that it surrounds all the four wall boundary layers inside the rectangular channel, being suspended at around 2mm from each wall surface. With this condition, the flow at the measurement position becomes turbulent flow in the transition region.

Table 2.5 Experimental conditions (Laminar-to-turbulent flow) (x/h=30)

Mean velocity of oil, U [m/s]	0.63	1.02	1.51	2.03
Mean void fraction: α [%]	0 to 2.5	0 to 2.5	0 to 2.5	0 to 2.5
Bubble diameter [mm]	0.8 to 4.5	0.7 to 3.2	0.7 to 2.1	0.5 to 1.2
Temperature [℃]	21	21	21	21
Density [kg/m^3]	935	935	935	935
Kinematic viscosity [mm^2/s]	10.66	10.66	10.66	10.66
Surface tension [mN/m]	20.1	20.1	20.1	20.1
$Re: UH/\nu,\quad H=2h$	1173	1793	2777	3734
$Re_\tau:\ U_\tau h/\nu$	36	46	56	64
$Fr:\ U(gh)^{-1/2}$	2.00	3.24	4.82	6.49
$We:\ \rho U^2 d/\sigma$	13 to 75	31 to 150	68 to 216	93 to 223
$We_\tau:\ \rho U_\tau^2 d/\sigma$	0.1 to 0.3	0.1 to 0.4	0.1 to 0.4	0.2 to 0.3
$We_{sh}:\ \rho(U/h)^2 d^3/\sigma$	0.1 to 15	0.2 to 16	0.3 to 17	0.2 to 3

Table 2.6 Experimental conditions (Laminar-to-turbulent flow) (x/h=90)

Mean velocity of oil, U [m/s]	0.63	1.02	1.51	2.03
Mean void fraction: α [%]	0 to 2.5	0 to 2.5	0 to 2.5	0 to 2.5
Bubble diameter [mm]	0.8 to 4.5	0.7 to 3.2	0.7 to 2.1	0.5 to 1.2
Temperature [°C]	20	20	21	22
Density [kg/m^3]	935	935	935	935
Kinematic viscosity [mm^2/s]	11.10	11.10	10.88	10.66
Surface tension [mN/m]	20.1	20.1	20.1	20.1
$Re: UH/\nu,\quad H=2h$	1126	1830	2777	3811
Re_τ: $U_\tau h/\nu$	36	46	56	64
Fr: $U(gh)^{-1/2}$	2.00	3.24	4.82	6.49
We: $\rho U^2 d/\sigma$	13 to 75	31 to 150	68 to 216	93 to 223
We_τ: $\rho U_\tau^2 d/\sigma$	0.1 to 0.3	0.1 to 0.4	0.1 to 0.4	0.2 to 0.3
We_{sh}: $\rho(U/h)^2 d^3/\sigma$	0.1 to 15	0.2 to 16	0.3 to 17	0.2 to 3

(3) Experimental results

Fig.2.21 shows the measurement results of friction coefficient as a function of Reynolds number. In Fig.2.21(b), the values at approximately U=2.5m/s are shown, in addition to those denoted in Table 2.6. The dot-dashed line in each graph indicates theoretical value for single-phase laminar channel flow and the dotted line indicates single-phase turbulent channel flow provided that the influence of sidewall is ignored. The theoretical friction coefficient for laminar channel flow is known by,

$$C_f = \frac{12}{R_e} \tag{2.5}$$

The friction coefficient of single-phase turbulent channel flow is known by,

$$\frac{R_e}{2} = \sqrt{\frac{2}{C_f}}\exp[\chi(\sqrt{\frac{2}{C_f}} - C_1 - C_2 + J)] \tag{2.6}$$

here, χ is Karman's invariant constant, and the other constants are given by C_1=55, C_2=0.7, and J=3.8. The measured data for the single-phase flow takes the laminar friction coefficient as Reynolds number is less than 3000, and then takes the turbulent friction coefficient as Reynolds number increases. The gap of the friction coefficient between the present measurement data and the theoretical value for the turbulent flow is caused probably by the limited aspect ratio of the channel, which is 8 in the present channel. In the case bubbles are mixed, the friction coefficient drastically increases in the originally laminar flow region. Moreover, the friction coefficient of the bubbly channel flow takes approximately the same value of the single-phase turbulent channel flow. This implies that the laminar flow is stimulated and altered into turbulent flow by mixing bubbles. On the other hand, the bubble's effect on the friction coefficient becomes minor in the originally turbulent flow region but a slight reduction of the friction can be confirmed. The slight difference in the data shown in the present graph and that shown in Fig.2.18(a) may be due to the absence and presence of trip wires for turbulence stimulation.

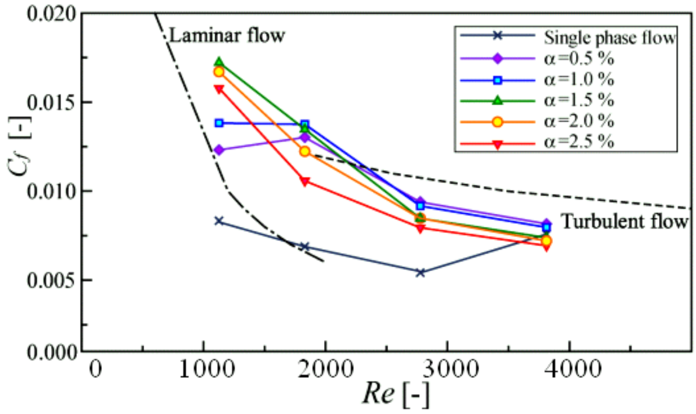

(a) x/h=30

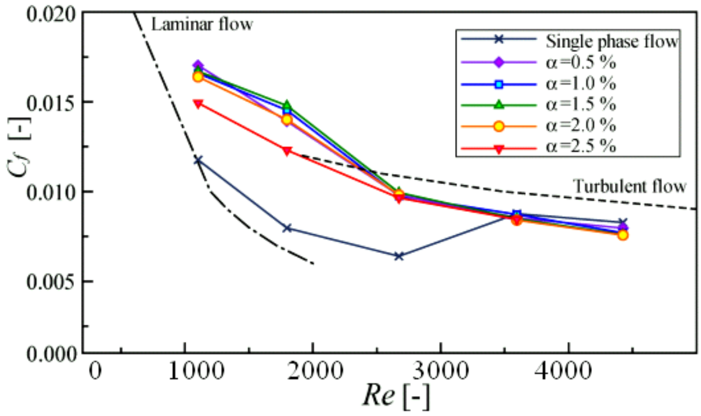

(b) x/h=90

Fig.2.21 Friction coefficient measured in the transition region

Fig.2.22 shows the skin friction ratio as a function of void fraction. When the liquid velocity U is slow, the ratio takes a value larger than unity but smaller than two. This ratio corresponds generally with the ratio of turbulent friction to laminar friction as shown before. However, the increment ratio is gradually reduced by increase of the void fraction. On the other hand, the ratio takes a value smaller than unity as the liquid velocity and the void fraction are given high simultaneously. In the case of the liquid velocity equal or larger than 2.0m/s (Re=3734 to 3811), the frictional reduction of 9 % is obtained in the maximum case. This fact tells us that the bubbles have a certain role to reduce the friction in such a low Reynolds number range as well.

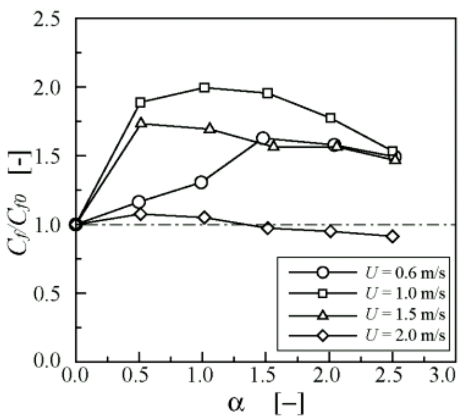

(a) x/h=30

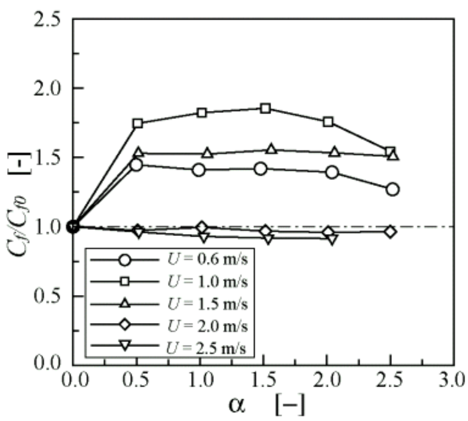

(b) x/h=90

Fig.2.22 Skin friction ratio versus void fraction beyond the transition

Fig.2.23 shows the pictures of bubbles in the channel, photographed at 900mm(x/h=90) from the bubble generator. The bubbles are nearly spherical at U=0.5m/s, but individual shape deforms as bubbles are densely suspended like foam. As the liquid velocity increases, the bubbles are elongated in the streamwise direction. The typical value of the aspect ratio (the ratio of the long axis to the short axis) is unity at U=0.5m/s, 2 at U=1.0m/s, and 5 at U=1.5m/s.

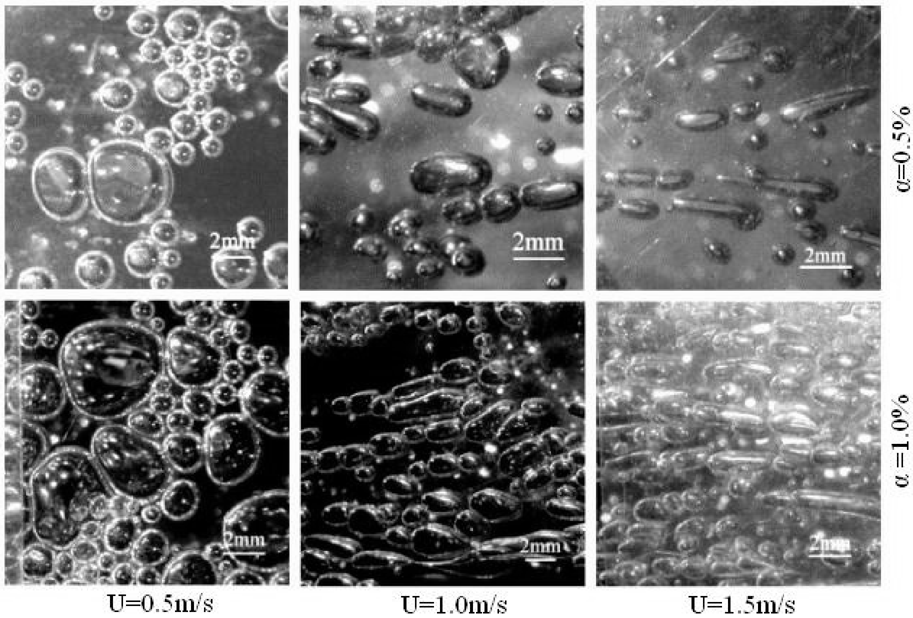

Fig.2.23 Bubbles in the channel (channel top view, flow is from left to right)

2.4 Summary of Chapter 2

Experimental measurements of bubbly two-phase channel flows are performed for two kinds of liquid media: one is water channel flow, and the other is Silicone oil channel flow. From the channel flow experimentations, following results are obtained:

- [Synchronized measurement] In the case of relatively large bubbles (d/h>1), there is a significant negative correlation between the local wall shear stress and the local void fraction. The local friction takes a high value in the front half of the bubble and a low value in the rear part. The local zero-friction point appears when the bubble length in the streamwise direction is longer than a critical value (which was around d/h=10).
- [PTV] The correlation $\alpha' v'$ produces a significant negative shear stress in the upper half of the channel, which contributes to the drag reduction. On the other hand, the triple correlation $\alpha' u' v'$ has a small positive stress. The negative stress $\alpha' v'$ originates from vertically oscillating bubbles which are observed frequently in the vicinity of top wall surface.
- [Silicone oil channel] The injection of bubbles provides increase in the friction coefficient less than 50% in the case of laminar channel flows. In the transition region from laminar to turbulent flows, the friction coefficient jumps up to double because bubbles activate the turbulent flow transition. The increment ratio of the friction coefficient matches the ratio of turbulent/laminar friction coefficients. After the transition to turbulent flow, the increment ratio is reduced gradually by increase in the void fraction. In the case that the flow is originally turbulent, the mixing of bubbles produces a certain drag reduction.

3. Numerical Simulation of Microbubble Channel Flow

3.1 Outline of the study

In order to compare directly with the experiment using silicone oil described in Chapter 2, Direct Numerical Simulations (DNS) are performed for microbubble channel flows. The calculation condition is set almost the same as the experimental condition using silicone oil. Turbulence statistics such as a modulation of turbulence production, which substantially affects a skin friction reduction or increase due to adding microbubbles, are discussed in detail.

Two kinds of numerical simulation methods are employed:(1) Force Coupling Method (FCM) and (2) Front-Tracking Method (FTM). In both the simulation methods, the grid size is smaller than the bubble diameter so that smaller scale flow structure is fully resolved. In the next section, numerical simulations using FCM are shown for laminar and turbulent cases. In the third section, numerical simulations using FTM are shown for the turbulent case.

3.2 Force-Coupling Method (FCM)

3.2.1 Introduction

In the present section, numerical simulations using FCM are shown for laminar and turbulent cases. In the simulation using FCM, which is developed by the group of Prof. Maxey (Maxey and Patel,2001; Lomholt *et al.*,2002), the bubble is treated as a sphere and the bubble-liquid interaction is simply represented by the body force. Xu *et al.*(2002) numerically obtained the microbubble drag reduction by the FCM simulation.

3.2.2 Numerical method

We assume the bubble is spherical and rigid. The basic equations are almost the same as those shown by Maxey and Patel (2001). The governing equations for the bubble motion are based on those given by Lomholt et al.(2002) and Xu et al. (2002). The governing equations for the liquid consist of the mass conservation equation given by

$$\nabla \cdot \vec{u} = 0 \tag{3.1}$$

and the momentum equation expressed as

$$\rho \frac{D\vec{u}}{Dt} = -\nabla p + \mu_L \nabla^2 \vec{u} + \vec{F}_p \tag{3.2}$$

where $\vec{F}_p$ represents the body force due to the bubble motion. Considering the force monopole and the force dipole, $\vec{F}_p$ is expressed as,

$$F_{pi} = \sum_{l=1}^{N_b} \left(F_i^{(l)} \Delta(\vec{x} - \vec{Y}^{(l)}, \sigma_m) + F_{ij}^{(l)} \frac{\partial}{\partial x_j} \Delta(\vec{x} - \vec{Y}^{(l)}, \sigma_d) \right) \tag{3.3}$$

where $\vec{Y}^{(l)}$ is the centroid position of the l-th bubble. The first term in the parentheses of the RHS denotes the force monopole term, and the second term denotes the force dipole term. As shown in Fig. 3.1 the force monopole term causes drag force in the uniform flow mode, and the force dipole term causes effective viscosity in the uniform shear mode. Δ is the Gaussian function and σ_m and σ_d are envelope scales for the force monopole and the force dipole respectively, as shown by Lomholt et al. (2002). In the present study, the calculation method for $F_i^{(l)}$ is based on that shown by Xu et al.(2002) and that for the antisymmetric part of $F_{ij}^{(l)}$ is approximated by the surface integral in the following way,

$$\frac{1}{2}(F_{ij}^{(l)} + F_{ji}^{(l)}) = \frac{5\mu_L a^{(l)}}{3} \oint_{|\vec{x} - \vec{Y}^{(l)}| = a} d^2 x S_{ij} \tag{3.4}$$

We checked the Couette flow with a spheroid particle by use of Eq.(3.4) and confirmed that the relation between the skin friction and the particle volume fraction shows good agreement with the Einstein's theory.

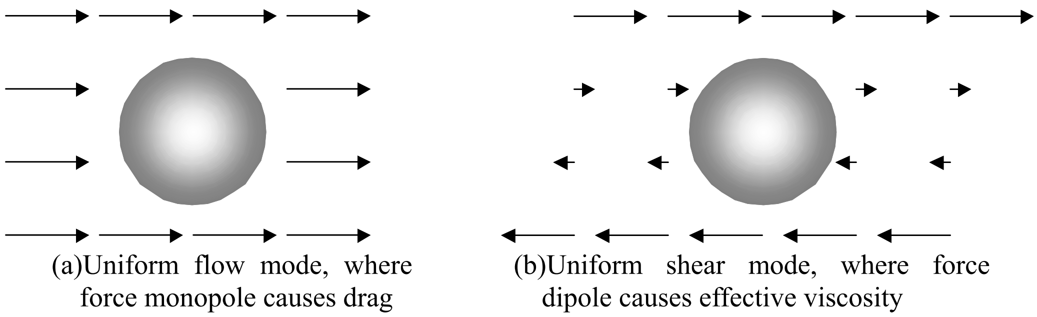

Fig. 3.1 Flow modes and the force terms

We modified the simulation codes to solve the buoyant bubble approaching the top wall while keeping numerical robustness. We performed the simulations under both laminar and turbulent flow situations and took long enough time to obtain the turbulence statistics.

Flow between two solid walls driven by a mean pressure gradient is computed. Fig. 3.2 shows the computational domain and the definition of the coordinate system. The *x*, *y*, and *z*-axes are taken in the streamwise, wall-normal and spanwise directions, respectively. A periodic condition is applied in *x*- and *z*-directions. The solution of the single phase flow simulation is used as the initial velocity field of the computation with bubbles.

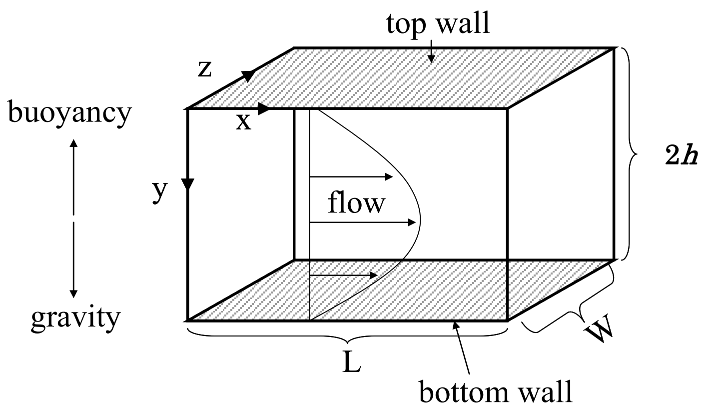

Fig. 3.2 Computational domain and definition of coordinate system.

The governing parameters are the Reynolds number *Re,* the ratio of the bubble diameter to the channel half height *d/h* and the Weber number *We.* The dimensionless numbers are defined as follows:

$$Re = \frac{2U_m h}{\nu}, \qquad We = \frac{\rho U_m^2 d}{\sigma}, \tag{3.5}$$

where U_m is the volume-averaged mean velocity of the mixture, ν is the kinematic viscosity of the liquid, ρ is the density of the liquid and σ is the surface tension. The Reynolds number based on the friction velocity Re_τ is related to the Reynolds number as

$$Re_\tau = \sqrt{\frac{C_f}{2}}\frac{Re}{2} \tag{3.6}$$

where C_f is the skin friction coefficient defined as,

$$C_f = \frac{\tau_w}{1/2\rho U_m^2} \tag{3.7}$$

in which τ_w is the average wall shear stress.

3.2.3 Simulation conditions

Table 3.1 shows the experimental conditions for laminar and turbulent flows targeted in the present numerical simulation using FCM for the air-Silicone oil system. The targeted kinematic viscosity of the Silicone oil in the experiment is slightly different from that shown in Table 2.1. Table 3.2 shows the derived non-dimensional parameters adopted in the numerical simulation.

The experimental conditions of the actual experiment using Silicone oil, shown in Tables 2.1, 2.2, 2.4, 2.5 and 2.6, do not agree completely with the targeted ones shown in Table 3.1. In the laminar flow case they agree, except that the mean void fraction is lower (up to 2.5%) in the actual experiment. As shown in Table 2.4 the mean (or bulk) flow speed of the actual experiment ranges from 0.5 to 1.5m/s, but for direct comparison with the numerical simulation, only the case U_m=0.5m/s should be used. In the turbulent flow case the experimental and simulation conditions agree with each other. As shown in Table 2.5 the mean (or bulk) flow speed of the actual experiment ranges from 0.63 to 2.03m/s, but for direct comparison with the numerical simulation, only the case U_m=2.03m/s should be used.

Table 3.1 Targeted experimental conditions using silicone oil (FCM, laminar & turbulent flows))

	Laminar flow	Turbulent flow
Channel half height h (m)	0.005 (A2-Channel)	0.01 (B2-Channel)
Mean bubble diameter d (m)	0.002	0.002
Mean void fraction α (%)	5	2.5
Mean flow velocity U_m (m/s)	0.5	2
kinematic viscosity ν (m^2/s)	10.0×10^{-6}	10.0×10^{-6}

Table 3.2 Simulation conditions (FCM, laminar & turbulent flows)

Parameters	Laminar flow	Turbulent flow
$R_e(=\dfrac{2U_m h}{\nu})$	500	4000
$\mathrm{Re}_\tau(=\dfrac{u_\tau h}{\nu})$	27.4	135
$W_e(=\dfrac{\rho d U_m^2}{\sigma})$	- (rigid)	- (rigid)
$F_r(=\dfrac{U_m}{\sqrt{gh}})$	2.26	6.39
d/h	0.4	0.2
L/h	2π	2π
W/h	π	π
Number of grid	64x64x64	64x64x64

3.2.4 Computed results

(1)Laminar Poiseuille flow

The position of the bubbles for the laminar flow case is shown in Fig.3.3. Initially, the bubbles are randomly distributed in the entire flow region as shown. As the time passes, the bubbles tend to appear in the upper region due to the buoyancy force.

The void fraction profile is shown in Fig.3.4. The peak of the void fraction moves toward the top wall as the flow evolves because of the buoyant motion of bubbles.

The time history of the friction coefficient C_f on the top and bottom walls is shown in Fig.3.5. With respect to the initial behavior (t<0.2(s)), the skin friction increases due to the presence of bubbles as compared with C_f with no bubble, Especially, C_f on the top wall considerably increases when the bubbles migrate toward the top wall. The skin frictions on both the top and bottom walls take their peak at the time of t~0.2(s). With respect to the long-time behavior (t>0.2(s)), the skin friction gradually decreases and approaches to that with no bubble. In the fully developed situation, the most bubbles reach the top wall and move along the wall. Thus, the liquid flow induced by the vertical motion of bubbles, which modulates the skin friction, attenuates in time.

The fact that skin friction increases with bubbles in the laminar flow condition agrees with the experimental result using Silicone oil (see Fig.2.18(a)). Comparison of the long-time behavior is not possible because the experimental information cannot be obtained.

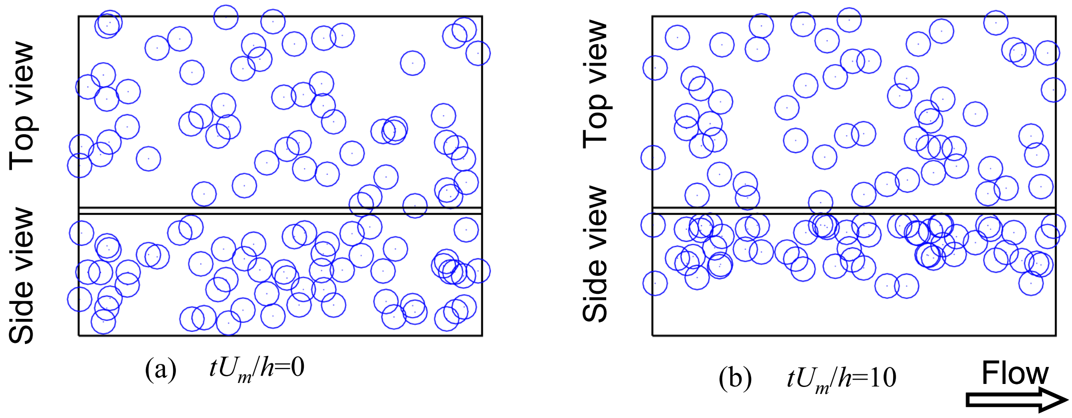

Fig. 3.3 Bubble distribution (FCM, Laminar flow)

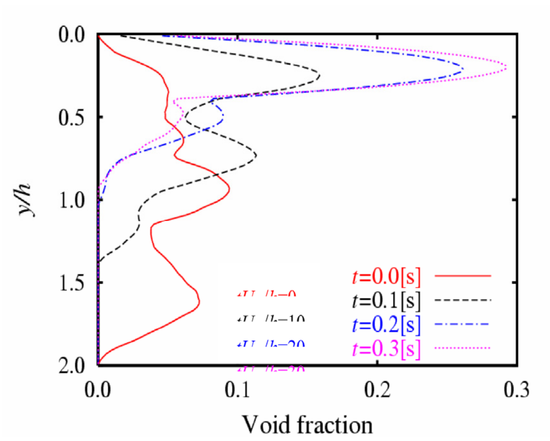

Fig. 3.4 Void fraction profile (FCM, laminar)

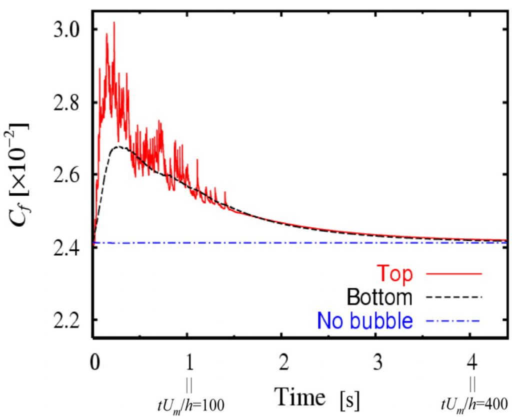

Fig. 3.5 Time history of friction coefficient (FCM, laminar)

The statistics in initial and fully developed stages are discussed. The mean velocity profile is shown in Fig.3.6. The lower figures show the change of the mean velocity by adding the bubbles. Figure 3.6(a) corresponds to an initial short-time statistic sampled from t=0 to t=1 (s), and Figure 3.6(b) corresponds to a fully developed statistic sampled from t=2 to t=4 (s), respectively. As shown in Fig.3.6(a), the initial velocity modulation is small but finite. The velocity profile is initially flattened in the upper region where bubbles accumulate. Such a flattened profile may be caused by the vertical motion of bubble. When the flow is fully developed, the mean velocity difference between the single phase and multiphase flows becomes almost zero.

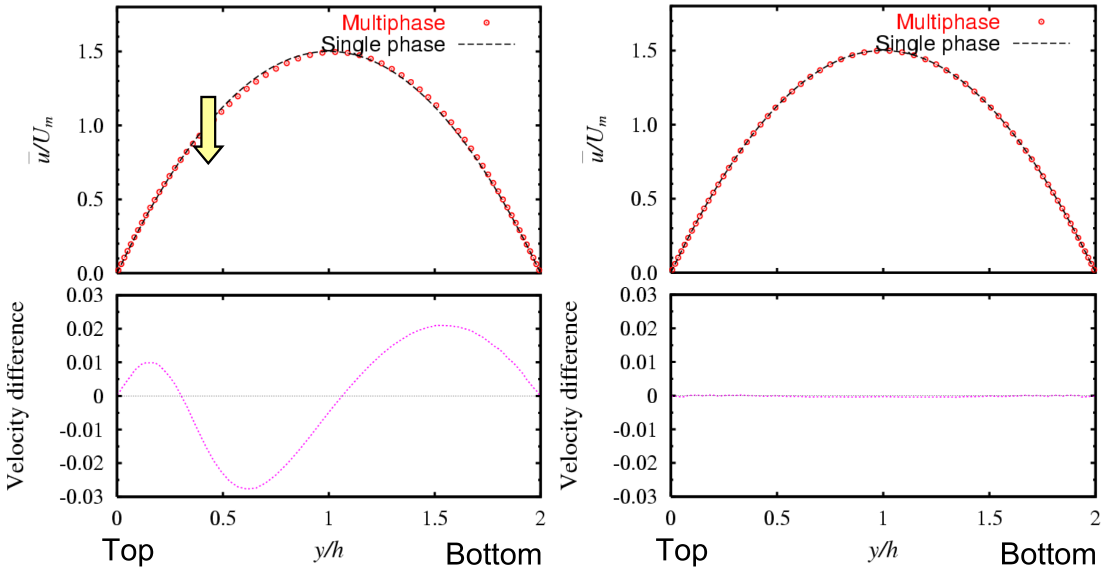

(a) $0<t<1$ (s)　　(b) $2<t<4$ (s)

Fig. 3.6　Mean velocity (FCM, laminar flow)

The turbulent intensities scaled by the mean velocity U_m are shown in Fig.3.7. Similarly to Fig.3.6, initial and fully developed statistics are plotted. As shown in Fig.3.6(a), the significant turbulence is initially induced by the vertical motion of the bubble in spite of the laminar flow. According to a dissipation theory for a microbubble flow shown by Sugiyama *et al*.(2004), the skin friction almost balances with the total dissipation rate. The initial increase of the skin friction shown in Fig.3.7(a) may be caused by an additional dissipation rate due to the turbulence induced by the bubble motion, i.e., so called the pseudo turbulence. On the other hand, the turbulent intensities become considerably small in the fully developed state as shown in Fig.3.7(b). The fully developed results shown in Figs. 3.6(b) and 3.7(b) indicate that the dynamic interaction between the gas and liquid phases is quite small.

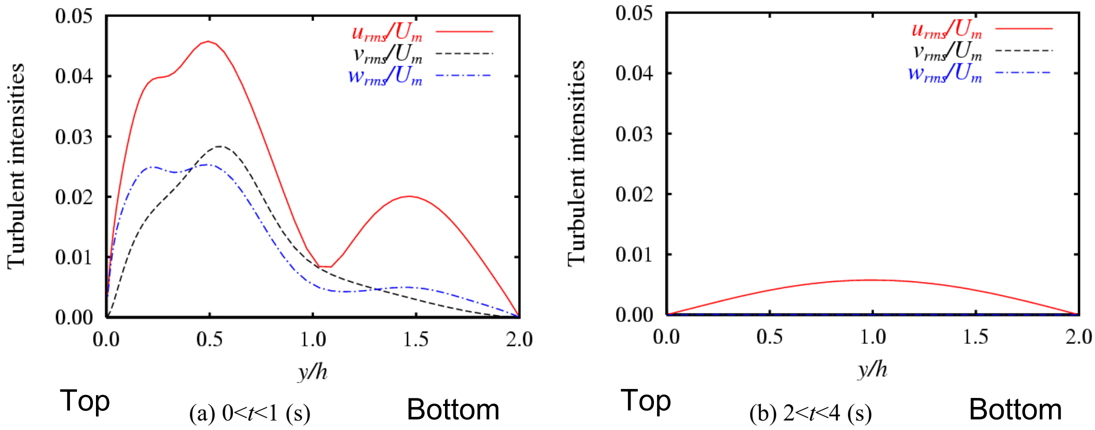

(a) $0<t<1$ (s)　　(b) $2<t<4$ (s)

Fig. 3.7 Turbulent intensities (FCM, laminar flow)

(2) Turbulent flow

In the experiment, the bulk Reynolds number Re is the flow parameter. However, U_m in Eq.(3.5), which corresponds to the velocity averaged over the entire region, cannot be prescribed without computation. In the numerical simulation of the channel flow, the driving pressure gradient is usually fixed ($-dP/dx=1$) and only the friction Reynolds number Re_τ is prescribed. In the present study, the empirical relation of $Re_\tau=0.09Re^{0.88}$ is used to determine the friction Reynolds number. As shown in Table 3.2, Re=4000 for a single phase flow corresponds to Re_τ=135. The bulk Reynolds number is actually evaluated as 4000 within a few percent error in the simulation.

The position of the bubbles for the turbulent flow case is shown in Fig.3.8. Initially, the bubbles are randomly distributed in the entire flow region as shown in Fig.3.8(a). Similarly to the laminar flow (see Fig.3.3), the bubbles tend to appear in the upper region as the flow evolves because of the buoyant motion of bubbles.

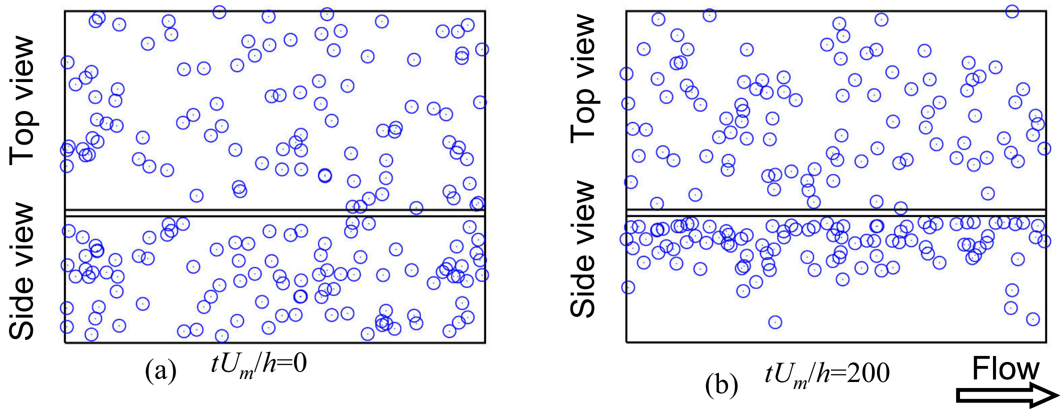

Fig.3.8 Bubble distribution (FCM, turbulent flow)

The void fraction profile for the turbulent flow case is shown in Fig.3.9. Similarly to the laminar flow case, the peak of the void fraction initially moves toward the top wall as the flow evolves. However, several bubbles are located below the center of the channel even in the fully developed time (t=2(s)). In the turbulent flow, not only the buoyancy but also the bubble dispersion are important factors to determine a number density of the bubble. Thus, the void fraction in the turbulent flow may have statistically steady profile due to the balance between the buoyancy and the dispersion.

The temporal evolution of the centroid of the bubbles' y-position in the channel is shown in Fig.3.10. The period shown in Fig.3.10 is long enough to sample the turbulence statistics. Although the centroid position initially moves to the top wall, it approaches a certain position (y/h~0.53) in the fully developed state. The length between thin lines in Fig.3.10 corresponds to the bubble diameter. The fact that the bubble centroid is located at y/h=0.53 shows that the gap between the top wall and the top edge of the bubble is much larger than the bubble diameter. The statistical fluctuation of the centroid position is small enough as compared with the bubble diameter. These behaviors of the centroid position indicate that the void fraction in the turbulent flow has statistically steady profile.

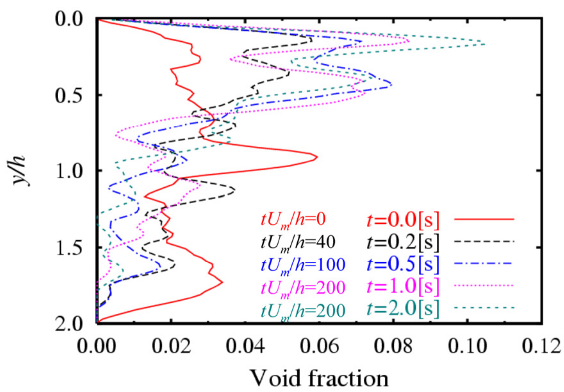

Fig.3.9 Void fraction profile (FCM, turbulent flow)

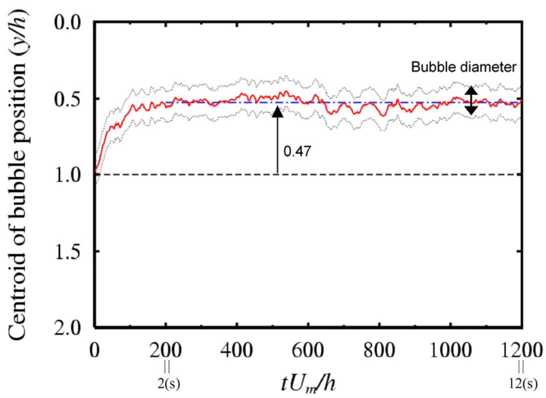

Fig.3.10 Centroid of bubble y-position (FCM, turbulent flow)

The mean void fraction profile is shown in Fig.3.11. The start time for sampling is tU_m/h=200 based on the temporal behavior of the centroid position shown in Fig.3.10. The sampling is carried out until tU_m/h=1200. The blue line corresponds to the centroid of the bubbles' y-position (y/h=0.53).

Above the blue line, two local peaks are recognized at y/h~0.15 and y/h~0.35. While the peak positions are not stable position where the bubble can steadily stay because of the turbulence, some mechanisms frequently to accumulate bubbles may exist. As shown later, the position y/h=0.35 corresponds to the location showing the maximum of the wall-normal component of the turbulent intensity. The mean pressure profile is given by $p = p_w - \rho v_{rms}^2$, where p_w is the mean pressure at wall. Thus, the position y/h=0.35 corresponds to the location showing the minimum pressure, where the bubbles are likely to accumulate. If the bubble's centroid is located at y/h=0.15, the clearance between the wall and the bubble is small ((y-d/2)/h=0.5) and the bubble almost touches the wall. Note that the repulsive force between the bubble and the wall is introduced to avoid the penetration in the numerical simulation. The reason to show the peak of the mean void fraction at y/h=0.15 is considered the balance between the buoyant and wall-repulsive motions of the bubble.

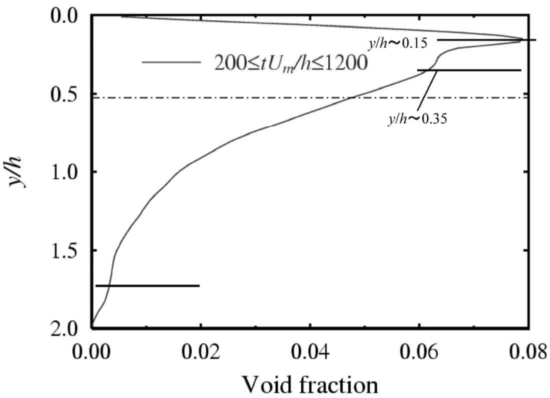

Fig.3.11 Mean void fraction profile (FCM, turbulent)

The time history of friction coefficient C_f on the top and bottom walls normalized by the value of the single phase flow C_{f0} for the turbulent case is shown in Fig.3.12. The scaled C_f fluctuates around the reference value with relatively about 10% fluctuation to C_{f0}. When averaging C_f/C_{f0} from tU_m/h=200 to 1200 by considering the void fraction profile, about 2.3% increase of the friction coefficient on the top wall can be recognized. On the other hand, the modulation of the skin friction on the bottom wall is quite small.

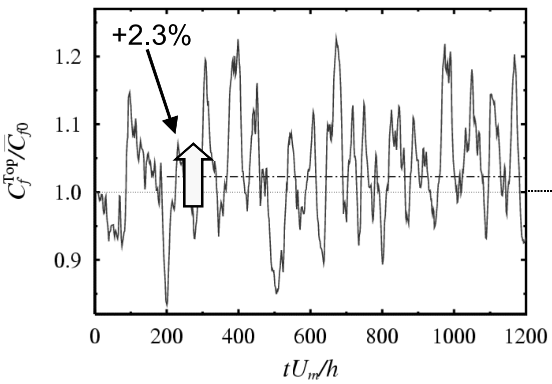

(a) Top wall

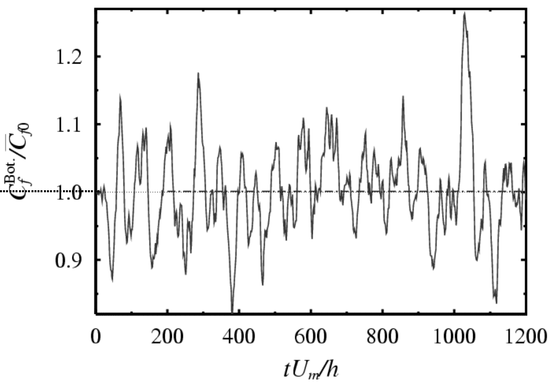

(b) Bottom wall

Fig. 3.12　Time history of friction coefficient (FCM, turbulent flow)

The mean velocity u/U_m profiles are shown in Fig.3.13. Fig.3.13(b) denotes the turbulent flow case computed by FTM (Front-Tracking Method), where bubbles are flexible and their deformation is taken into account (see Section 3.3). The solid and chain lines correspond to the liquid velocities in the multiphase and single-phase flows, respectively. The symbol in Fig.3.13(c) corresponds to the mean velocity of the bubbles. As compared between (a) and (b) in Fig.3.13, the tendency of the velocity modulation for the turbulent flow case with spherical, rigid bubble is similar to that for the turbulent flow case with deformable bubbles. The mean velocity becomes asymmetric due to the asymmetric bubble distribution. As shown in Fig.3.13, the mean velocity in the multiphase flow becomes smaller than that in the single phase flow in the upper half of the channel where the void fraction is high. It is seen from Fig.3.13(c) that the mean velocity of the bubble is also smaller and the deviation from the velocity in the single phase flow is larger than that of the liquid. Thus, the liquid motion may be dragged by the slow bubbles in the high void fraction region. Consequently, the mean velocity gradient decreases in the buffer layer (y/h<0.2). Such a decrease of the mean velocity is also observed in the initially transient state of the laminar flow (see Fig.3.6).

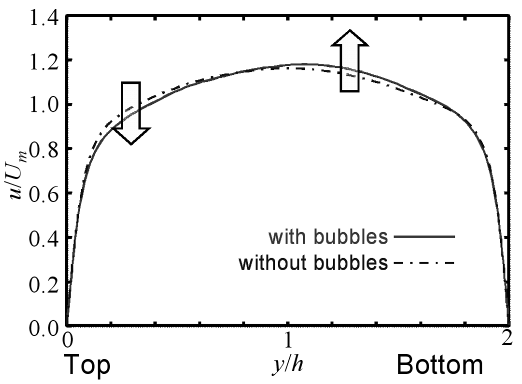

(a)FCM

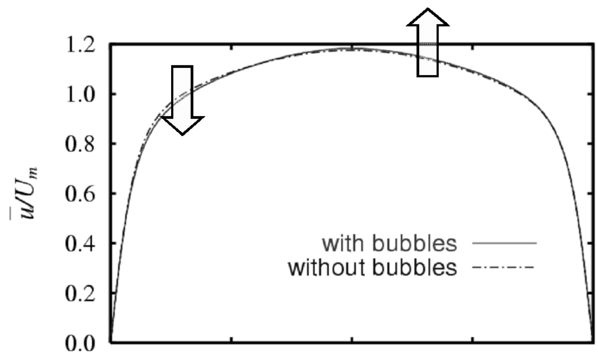

(b)FTM

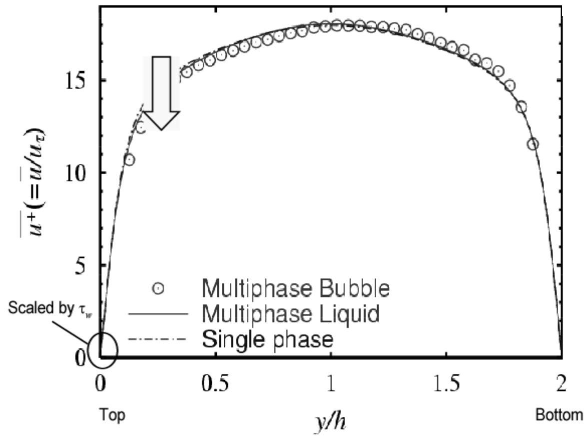

(c) Bubble velocity (FCM)

Fig. 3.13 Mean velocity profile (FCM & FTM, turbulent flow)

The profile of the Reynolds shear stress for the turbulent flow case is shown in Fig.3.14. The Reynolds shear stress, i.e., velocity fluctuation $-u'v'$ of the bubble is much smaller than that of the liquid. This is because the bubble diameter is much larger than the energy-contained eddy size and the bubble motion becomes dull compared with the liquid motion. However, the modulation of the Reynolds shear stress of the liquid due to adding the bubbles is small.

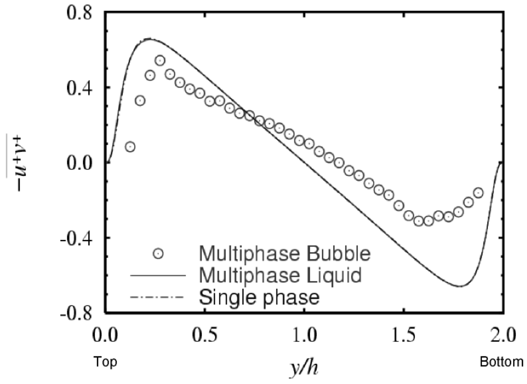

Fig. 3.14 Reynolds stress profile (FCM, turbulent)

The turbulent intensity profile for the turbulent case is shown in Fig.3.15. Similarly to the result shown in Fig.3.14, all components of the turbulent intensities of the bubble are much smaller than those of the liquid. As shown in Fig.3.15, the streamwise component of the turbulent intensity of the liquid in the multiphase flow becomes smaller than in the single phase flow in the upper half of the channel where the void fraction is high, while the wall-normal and spanwise components becomes larger. This result indicates that the turbulence is homogenized by the presence of bubbles. As shown in Fig.3.16, such a homogenization is also observed in the turbulent case with deformable bubbles.

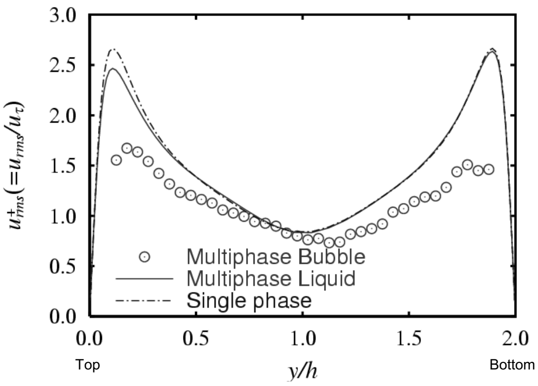

(a) streamwise component

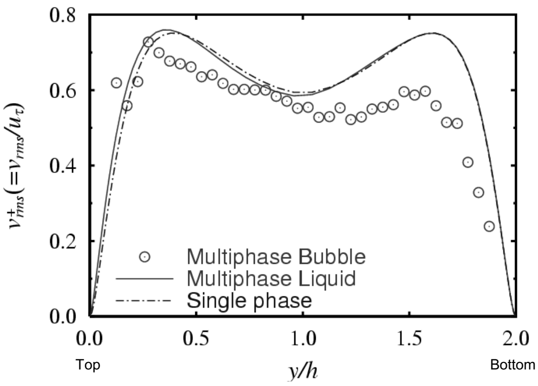

(b) wall-normal component

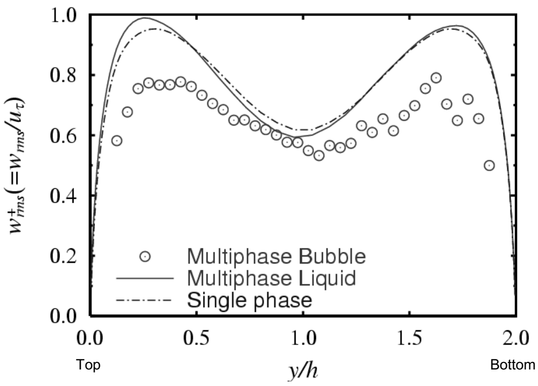

(c) spanwise component

Fig. 3.15 Turbulence intensities (FCM, turbulent flow)

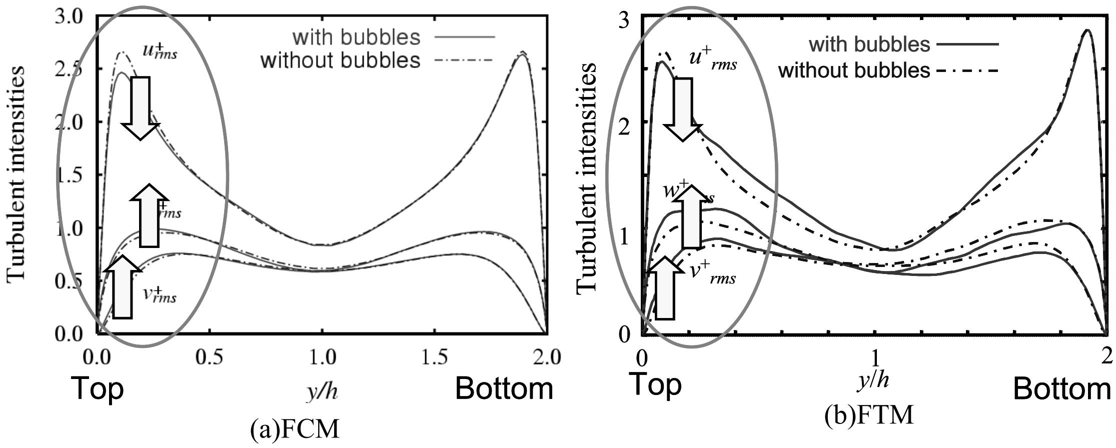

Fig. 3.16 Turbulence intensities (FCM & FTM, turbulent flow)

3.2.5 Summary of Section 3.2

Direct Numerical Simulations using FCM (Force Coupling Method) are performed for the channel flow with spherical, rigid bubbles in the laminar flow case (Re=500, Re_τ=27.4) and in the turbulent flow case (Re=4,000, Re_τ=135). The following results are obtained:

- In the laminar flow case, pseudo turbulence, which initially induced by bubbles' motion disappears as the flow evolves. The bubbles, initially distributed evenly in the channel, migrate toward the top wall due to buoyancy. In the fully developed stage, the mean velocity distribution becomes almost identical to that of the single phase flow. The skin friction increases with bubbles by approximately 20% in the initial stage. This tendency agrees with the experimental result using Silicone oil (see Fig.2.18(a)), except that the increase is about twice in the actual experiment. Comparison of the long-time behavior is not possible because the experimental information cannot be obtained.
- In the turbulent flow case, the skin friction increases by adding bubbles. The streamwise mean velocity component becomes smaller, due to the smaller bubble speed. The streamwise velocity fluctuation component becomes smaller and the wall-normal and spanwise components become larger, resulting in the tendency toward homogenization of the three velocity fluctuation components. The fluctuation velocities of the bubble are much smaller than those of the liquid. The gradient of the mean streamwise velocity attenuates in the high void fraction region.
- The modulations of the mean velocity and the turbulent intensities for spherical bubbles shows similar trend to those for deformable bubbles (FTM).

3.3 Front-Tracking Method (FTM)

3.3.1 Introduction

In the present section, numerical simulations using FTM are shown for the turbulent case. The FTM is generalized by Unverdi and Tryygvason (1992). In the FTM, the moving interface problem between two fluids is solved with rectangular grid system. The local boundary condition is more rigorously treated than that in the FCM. Especially, we can capture the bubble deformation. By using the FTM, we can perform the DNS of the microbubble flow. We have employed the FTM code developed by Kawamura and Kodama (2002). This code is numerically robust enough to reproduce the microbubble flow in the turbulent situation. In the experiment, the significant bubble deformation is observed. We can discuss the effect of bubble deformation on the skin friction reduction by checking the difference and analogy between the results of FTM and FCM.

Direct numerical simulations of low Reynolds number turbulent bubbly channel flow corresponding to B2-Channel in the experiment (see Table 2.2) and homogeneous turbulent shear flow containing bubbles have been performed using the front-tracking method. The purposes of this numerical study are to investigate the influence of the bubble deformation on the Microbubble Drag Reduction (MDR), and to validate the DNS through direct comparison with the experiment at low Reynolds numbers.

3.3.2 Numerical method

(1) Governing equations

Both water and air phases are treated as incompressible fluids, and the continuity of stress is implemented at the interface. The governing equations for each phase is the Navier-Stokes equation,

$$\frac{\partial u_i}{\partial t} = -\frac{\partial u_i u_j}{\partial x_j} + \frac{\partial}{\partial x_j}\left\{ \nu \left(\frac{\partial u_i}{\partial x_j} + \frac{\partial u_j}{\partial x_i} \right) \right\} - \frac{1}{\rho}\frac{\partial p}{\partial x_i} \tag{3.8}$$

and the continuity equation

$$\frac{\partial u_i}{\partial x_i} = 0 \tag{3.9}$$

where x_i , u_i , and p are the Cartesian coordinate, the velocity components, and static pressure respectively. The fluid density ρ and the kinematic viscosity ν take values of either water or air depending on whether the center of the computational cell is water or air.

(2) Outline of FTM

There are several methods for expressing the moving interface between two fluids, such as the VOF method, the level-set method, and the front-tracking method (Unverdi and Tryggvason, 1994). The VOF and level-set methods are categorized as the front capturing methods which track the movement of volume and find the interface in an indirect way. One of the merits of the methods of this type is that collision and breakup of interfaces are easily treated. On the other hand, the front-tracking method tracks the interface directly allowing more accurate calculation of the curvature of the interface, although treatment of surface re-structuring is complicated. We use the front-tracking method, since accurate calculation of the interface curvature is very important for the case investigated in this study.

Each bubble is expressed by its center position and radius distribution around the center as shown in Fig.3.17. Marker particles are placed on each bubble regularly on a two-dimensional spherical grid (θ,φ). In the beginning of each time step, the positions of the marker particles are updated using the velocity interpolated from the rectangular grid for solving the Navier-Stokes equations. After the marker particles are moved, the radius at each point $r(\theta,\varphi)$ is calculated and expanded in a series of spherical harmonic function,

$$r(\theta,\varphi) = \sum_{n=0}^{N}\sum_{m=0}^{n} \{A_{nm}\cos m\varphi + B_{nm}\sin m\varphi\} P_{nm}(\cos\theta) \tag{3.10}$$

in which N is the number of the deformation modes considered, P_{nm} is Legendre associate polynomial. N is set to 8 in this study. The coefficients A_{nm} and B_{nm} are obtained as follows:

$$A_{n0} = \frac{2n+1}{4\pi} \int_{-\pi}^{\pi}\int_{0}^{\pi} r(\theta,\varphi) P_{n0}(\cos\theta)\sin\theta\, d\theta d\varphi \tag{3.11}$$

$$B_{n0} = 0 \tag{3.12}$$

$$A_{nm} = \frac{2n+1}{2\pi}\frac{(n-m)!}{(n+m)!} \times \int_{-\pi}^{\pi}\int_{0}^{\pi} r(\theta,\varphi)\cos m\varphi P_{nm}(\cos\theta)\sin\theta\, d\theta d\varphi \tag{3.13}$$

$$B_{nm} = \frac{2n+1}{2\pi}\frac{(n-m)!}{(n+m)!} \times \int_{-\pi}^{\pi}\int_{0}^{\pi} r(\theta,\varphi)\sin m\varphi P_{nm}(\cos\theta)\sin\theta\, d\theta d\varphi \tag{3.14}$$

The primary merit of this method is that the curvature of the interface is accurately computed with relatively small number of grid points. Another advantage is that deformations of high wave number modes, which give rise to numerical instabilities, can be filtered out. Whereas the shortcomings are that the radius must be a single-valued function of the altitude and latitude (θ,φ) . Therefore, this method cannot deal with deformations beyond a certain limit, collision or separation of bubbles.

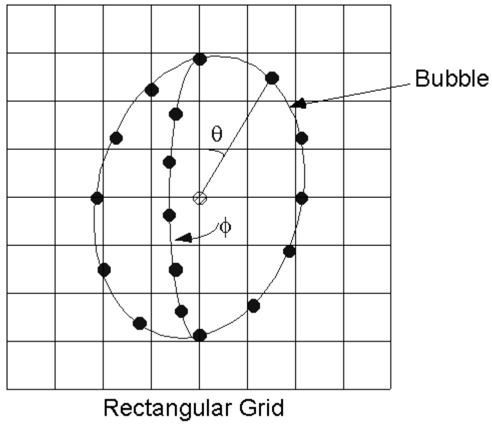

Fig. 3.17 Schematic sketch of the present Front-Tracking Method (FTM)

(3) Solution algorithm

A second-order finite volume method is used for the spatial discretization on a rectangular grid system fixed to the space, and a second-order semi-implicit fractional step method is used for the time integration. At the beginning of each time step, the positions and shapes of bubbles are determined, and the values of density and the kinematic viscosity in each cell are set to values of water or air. Whether a cell-center point is inside a bubble or not can be judged from Equation (3.10). Then the dynamic boundary condition is set in cells containing interfaces. The surface tension is treated as a pressure jump across the interface. The curvature of the interface is calculated from the Equation (3.10) analytically. Using this interface boundary condition the momentum equations (3.8) are semi-implicitly integrated, and then corrected by solving a Poisson equation for the pressure. The Poisson equation for the pressure is solved by a multigrid method.

More detailed description of the method and validation for a single rising bubble in stagnant fluid are found in Kawamura and Kodama (2002).

3.3.3 Computed results for turbulent flow

A fully developed turbulent channel flow containing bubbles is investigated by the present numerical method. Before introducing the bubbles, a fully developed single-phase turbulent channel flow at the Reynolds number Re_τ=110, based on the friction velocity u_τ and a half width of the channel h, was computed. The size of the computational domain is set to $6.4h \times 2h \times 3.2h$, in the streamwise, wall-normal and spanwise directions respectively. A periodic boundary condition is used in the streamwise and spanwise directions. The x-, y- and z- axes are taken in the streamwise, wall-normal and spanwise directions respectively as shown in Fig. 3.18. The profiles of computed mean velocity and turbulence intensity agree well with the DNS database of Iwamoto et al (2002) as shown in Fig. 3.19.

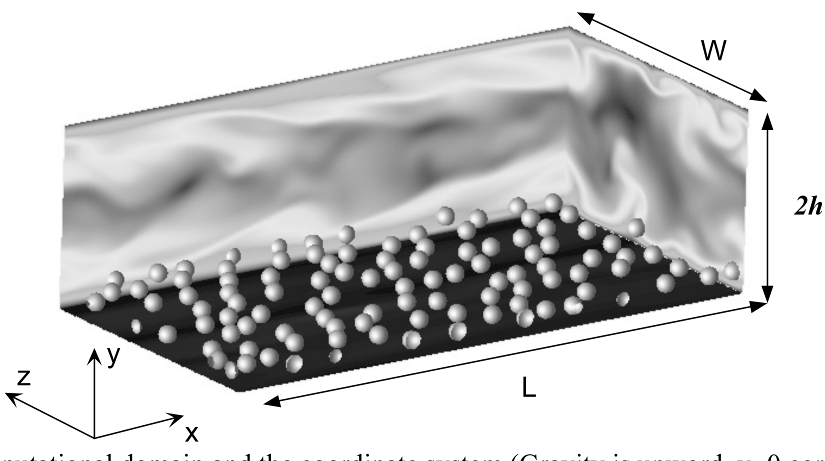

Fig. 3.18 Computational domain and the coordinate system (Gravity is upword, y=0 corresponds to the top wall in experiment) (FTM, turbulent flow)

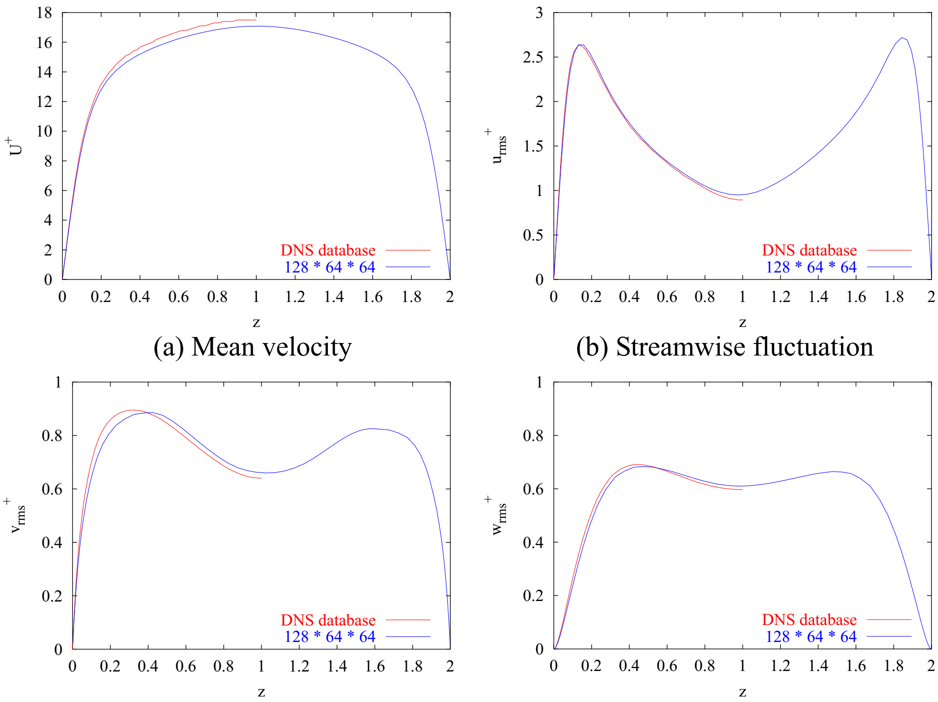

(a) Mean velocity　(b) Streamwise fluctuation

(c) Spanwise fluctuation　(d) Wall-normal fluctuation

Fig. 3.19 Validation of the single phase flow DNS (FTM, turbulent flow)

The limitations in the bubbly flow computation are the Reynolds number, the bubble size, the bubble deformation, and the bubble number. The present numerical method requires that bubbles are well resolved by the computational mesh, and deformation is moderate (Kawamura and Kodama, 2002). Therefore, the experiment using silicone oil and the B2-Channel was chosen as the target of the simulation. The targeted experimental conditions are summarized in Table 3.3, while the condition of the numerical computations is listed in Table 3.4. The volumetric flow rate is kept constant by automatically adjusting the mean pressure gradient. Table 3.5 shows comparison of simulation conditions with those of FCM. Compared to FCM, the Reynolds number and the Froude number are slightly lower and the void ratio is lower. The Weber number *We* is 50 and 100. Although the computation at *We*=200 was tried, it blew up before sufficient computational time was obtained. The number of grid points is twice to 16 times larger. The computation time of FTM is up to t^+=1,800, while that of FCM is t^+=3,645. The relation between t^+ and another non-dimensional time t^n is

$$\frac{t^+}{t^n} = 2\frac{\mathrm{Re}_\tau^2}{R_e} \tag{3.15}$$

Table 3.3 Targeted experimental conditions using Silicone oil (FTM, turbulent flow)

Silicone Oil + Air		B2-Channel
Parameters	Unit	Case3
U_m : Mean liquid velocity	m/s	1.5
s: Surface tension	N/m	0.021
r : Density of liquid	kg/m3	935
g : Acceleration of gravity	m/s2	9.806
h : Channel half height	m	0.010
n : Kinematic viscosity	m2/s	1.0E-05
d : Mean bubble diameter	m	0.002
a: Bulk-mean void fraction		0.01
Re=U_m*(2h)/n		3000
Cf0: Blasius' friction coeff.		0.0107
U_t: Blasius' friction velocity	m/s	0.1097
Re_t=U_t*h/n		110
We=r*U_m^2*d/s		200.36
We_t=r*U_t^2*d/s		1.071
We_s=r*U_m^2*d^3/(h^2*s)		8.014
Fr=U_m/sqrt(g*h)		4.79

Table 3.4 Simulation conditions of each calculation run (FTM, turbulent flow)

Calculation	RUN1	RUN2	RUN3	RUN4	RUN5	RUN6	RUN7	RUN8	RUN9	RUN10	RUN11
U_m : Mean liquid velocity	0.8413	0.8413	0.8413	0.8413	0.8413	0.8413	0.8413	0.8413	0.8413	0.8413	0.8413
s: Surface tension	0.000707	0.001416	0.002831	0.005662	0.014156	0.001413	0.001887	0.002831	0.005662	0.011325	0.005662
r : Density of liquid	1	1	1	1	1	1	1	1	1	1	1
g : Acceleration of gravity	0.030848	0.030848	0.030848	0.030848	0.030848	0.030848	0.030848	0.030848	0.030848	0.030848	0.030848
h : Channel half height	1	1	1	1	1	1	1	1	1	1	1
n : Kinematic viscosity	0.000561	0.000561	0.000561	0.000561	0.000561	0.000561	0.000561	0.000561	0.000561	0.000561	0.000561
d : Mean bubble diameter	0.2	0.2	0.2	0.2	0.2	0.4	0.4	0.4	0.4	0.4	0.4
a: Bulk-mean void fraction	0.010	0.010	0.010	0.010	0.010	0.011	0.011	0.011	0.011	0.011	0.032
Re=U_m*(2h)/n	3000	3000	3000	3000	3000	3000	3000	3000	3000	3000	3000
Cf0: Dean' friction coeff.	0.009864	0.009864	0.009864	0.009864	0.009864	0.009864	0.009864	0.009864	0.009864	0.009864	0.009864
Re_t=U_t*h/n	105.341	105.341	105.341	105.341	105.341	105.341	105.341	105.341	105.341	105.341	105.341
Fr=U_m/sqrt(g*h)	4.79	4.79	4.79	4.79	4.79	4.79	4.79	4.79	4.79	4.79	4.79
We=r*U_m^2*d/s	200.36	100	50	25	10	200.36	150	100	50	25	50
dpdx	0.004932	0.004932	0.004932	0.004932	0.004932	0.004932	0.004932	0.004932	0.004932	0.004932	0.004932
N : Bubble Number	98	98	98	98	98	13	13	13	13	13	39
L : Domain length	6.4	6.4	6.4	6.4	6.4	6.4	6.4	6.4	6.4	6.4	6.4
W: Domain width	3.2	3.2	3.2	3.2	3.2	3.2	3.2	3.2	3.2	3.2	3.2
Nx : Number of cells in x	256	256	256	256	256	128	128	128	128	128	128
Ny : Number of cells in y	128	128	128	128	128	64	64	64	64	64	64
Nz : Number of cells in z	128	128	128	128	128	64	64	64	64	64	64

Table 3.5 Simulation conditions: comparison with FCM (FTM, turbulent flow).

	FTM	FCM (Table 3.2)
$R_e(=\dfrac{2U_m h}{\nu})$	3,000	4,000
$\mathrm{Re}_\tau(=\dfrac{u_\tau h}{\nu})$	105.3	135
$W_e(=\dfrac{\rho d U_m^2}{\sigma})$	50, 100, (200)	- (rigid)
$F_r(=\dfrac{U_m}{\sqrt{gh}})$	4.79	6.39
d/h	0.4, 0.2	0.2
α (%)	1	2.5
L/h	6.4	2π
W/h	3.2	π
Number of grid	128x64x64, 256x128x128	64x64x64

$t^n (= \frac{tU_m}{h})$	(244)	400
$t^+ (= \frac{tu_\tau^2}{\nu})$	1,800	(3,645)

The simulation of the bubbly channel flow was initialized by a fully developed single phase flow, and compared with the flow instance which was continued without bubble seeding. The bubble centers are located a diameter away from the one wall (the upper wall in the experiment), and dispersed gradually by the turbulence.

Although the Weber number in the experiment was about 200, the computation at this Weber number was not possible due to heavy deformation of bubbles. The heavy deformation is also confirmed in the photographs taken in the experiment. Therefore computations were carried out at smaller Weber numbers.

The change of the friction coefficient on the bottom (with bubbles) and top (without bubbles) walls are shown in Fig. 3.20(a) and (b), respectively. Although the bubbly flow has not fully developed yet, it is noticed that at the bottom wall where bubbles are clustered the bubble seeding tends to slightly increase skin frictional at We=50 and slightly decrease skin friction at We=100. At the top wall which is bubble-free, the bubble seeding increases skin friction in both cases. The increase of the frictional drag is larger at We=50 than at We=100. This fact suggests that bubble deformation of bubbles reduces the effect of the bubble seeding, i.e. skin friction increase.

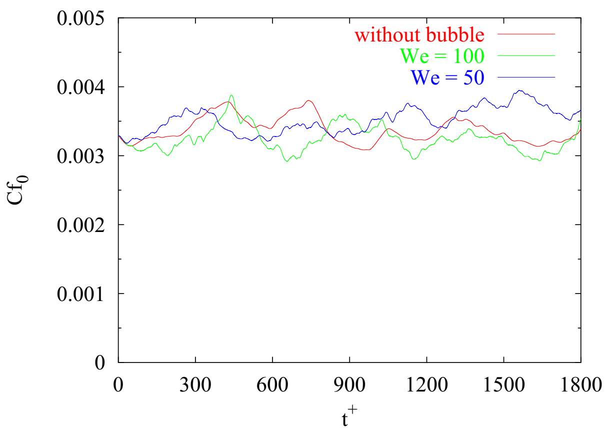

(a) Bottom wall (y=0).

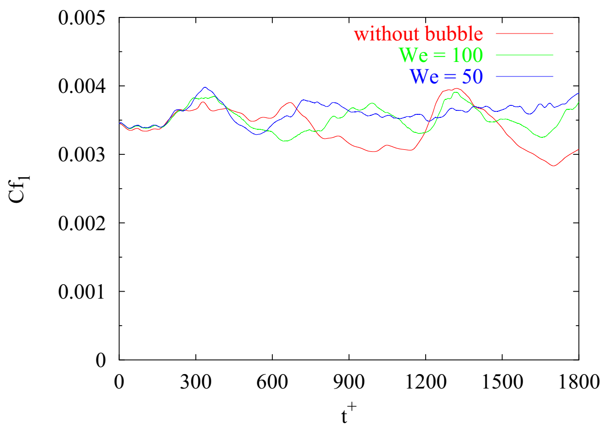

(b) Top wall (y=2)

Fig. 3.20 Time history of the friction coefficient. d=0.4 and α= 1%. (FTM, turbulent flow)

Fig. 3.21 shows the comparison of the Reynolds stress profiles with and without bubbles, in which the wall with bubbles corresponds to z=0. It is clearly indicated that the presence of bubbles increases the Reynolds stress. This is consistent with the increase of the friction coefficient shown in Fig. 3.20 and Fig. 3.21.

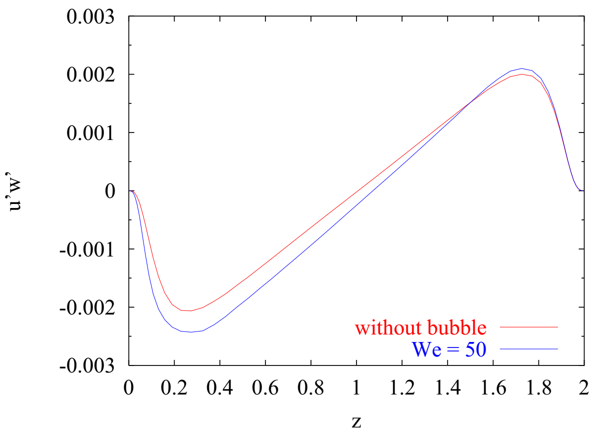

Fig. 3.21 Reynolds stress profiles. d=0.4, α=1%. (FTM, turbulent flow).

Fig. 3.22 shows the snap shots of the bubbles at three different Weber numbers. It is noticed that the deformation of bubbles becomes stronger as the Weber number is increased. At We=200, the computation broke up soon after the snap shot.

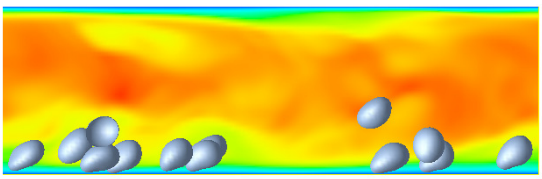

(a) We = 50

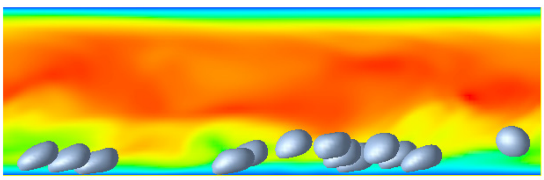

(b) We = 100

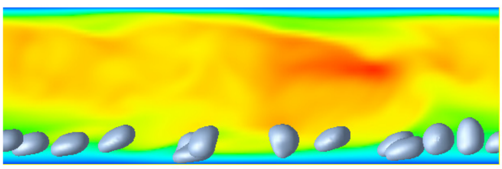

(c) We = 200

Fig. 3.22 Influence of the Weber number on the bubble deformation (d=0.2)

3.3.4 Summary of Section 3.3

Direct Numerical Simulations using FTM (Front-Tracking Method) are performed for the channel flow with deformable bubbles in the turbulent flow case (R_e=3,000, $R_{e\tau}$=105.3). The following results are obtained.

- The computation of bubble cases for a time sufficiently long to get statistical values was possible only up to We=100 because the computation blows up due to excessive bubble deformation.
- The skin friction tends to increase by adding less deformable bubbles (We=50) and decrease by adding more deformable bubbles (We=100), although the tendency is not very clear. Therefore it may be stated that, although at this low Reynolds number added bubbles increase skin friction, deformable bubbles have smaller contribution to the skin friction increase.
- The Reynolds stress increases by adding less deformable bubbles (We=50), which agrees with the tendency of the skin friction.

4. Numerical Simulation of Turbulent Homogeneous Shear Flow Using FTM

4.1 Introduction

The objective of the present study is to clarify the mechanisms of not only the drag reduction but also the drag increase by adding the microbubbles and to quantify the influence of parameters by means of the DNS. Such a parametric study is important to optimize the MDR in applications. However, the channel flow containing bubbles requires a lot of computational time in the numerical simulation so that this flow is not appropriate for the parametric study. Instead of the channel flow, the homogeneous turbulent shear flow containing bubbles is subjected. This flow has uniform shear and no solid boundary. The turbulence grows due to the dynamic interaction between the uniform shear and the turbulent eddy. This growth is caused by the superiority of the turbulence production term expressed by the product of the mean shear and the Reynolds shear stress to the turbulence dissipation term that suppresses the turbulence intensity. The homogeneous turbulent shear flow is considered the simplest one appropriately to investigate the vortical structure to generate the Reynolds shear stress. As quantified by Fukagata *et al*. (2002), the Reynolds shear stress is important for the skin friction in the wall bounded flow. From the dissipation theory for the microbubble flow (Sugiyama *et al*., 2004), the skin friction modulation due to the turbulence can be expressed by the change of the turbulence production in the whole region. On the similarity to the channel flow, the homogeneous turbulent shear flow often contains the equivalent vortical structures to those observed in the channel flow, such as the hairpin vortex in the logarithmic region and the streaky structure in the viscous sublayer (Rogers and Moin, 1987; Lee *et al*.,1990). Moreover, there is wide knowledge on the homogeneous turbulent shear flow. In the present study, the modulation of the turbulence production due to the bubble addition will be discussed by extracting the partial structure of the channel flow as shown in Fig.4.1. Especially, we will pay attention to the eddy structure.

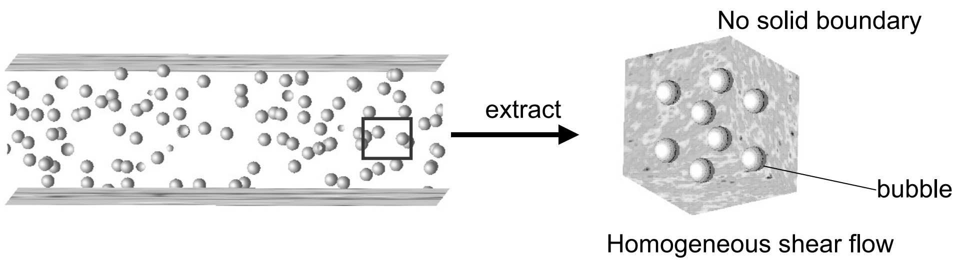

Fig. 4.1　Relation between channel flow and homogeneous shear flow

4.2 Numerical methods

The DNS of the homogeneous shear flow is performed based on the FTM code developed by Kawamura and Kodama (2002) for deformable bubbles. The finite volume method is used to discretize the governing equation in the fixed Cartesian coordinates. The size of the simulation domain is set to $L_x \times L_y \times L_z = 1\times1\times1$ (see Fig.4.2) divided by $N_x \times N_y \times N_z = 64 \times 64 \times 64$ or $128 \times 128 \times 128$ grid points, in the streamwise (x), spanwise (y) and normal (z) directions, respectively. There is no wall in the flow, thus the periodic boundary condition is imposed in x- and y-directions and the shear-periodic boundary condition (Gerz *et al.*,1989) in z-direction. The schematic figure of the shear-periodic boundary condition is shown in Fig.4.3. Its periodicity is satisfied by considering the displacement between the top (z=L_z) and bottom (z=0) domains due to the uniform shear in time. The shear rate S(=dU/dz) is set to 1 and the average velocity is expressed as U=(S(z-0.5), 0, 0).

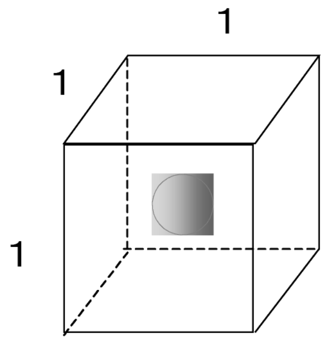

Fig. 4.2 Computational domain

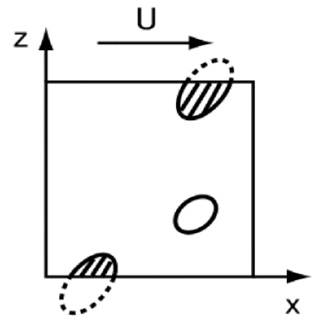

Fig. 4.3 Schematic figure of shear- periodic boundary

Initial turbulent field is randomly given by the solenoidal velocity vector satisfying the prescribed energy spectrum. The energy spectrum employed is the three-dimensional one E(k) proposed by Gerz. *et al.*(1989), which is given by,

$$E(k) = ak \exp\left(-\frac{k}{k_p}\right) \tag{4.1}$$

where k is wave number and k_p(=6) is the peak wave number.

The important parameters in this flow are the shear Reynolds number Re and the turbulent Reynolds number Re_t, which are define as follows:

$$\mathrm{Re} = \frac{Sd^2}{\nu} \tag{4.2}$$

and

$$\mathrm{Re}_t = \frac{u_{rms} d}{\nu} \tag{4.3}$$

in which S is the shear rate, d is the equivalent bubble diameter, and u_{rms} is the root mean square velocity fluctuation. The shear Reynolds number Re indicates the magnitude of the mean velocity gradient, while the turbulent Reynolds number Re_t is the measure of the turbulent intensity. It should be noted that the shear Reynolds number is a given parameter, while the turbulent Reynolds number varies with the growth or decay of the turbulence. If the surface energy is ignored, the budget of the turbulent kinetic energy K can be written as

$$\dot{K} = P - \varepsilon \tag{4.4}$$

where P is the production term

$$P = -S\overline{uw} \tag{4.5}$$

The temporal characteristic of the homogeneous shear flow is briefly described. The temporal evolution of the turbulent kinetic energy K is shown in Fig.4.4. K is normalized by its initial value K_0. As shown in Fig.4.4, K decreases in time at the initial state (t=0-2), while K increases exponentially at the fully developed state (t>2). The balance equation for the time derivative of K is expressed as,

$$\frac{\mathrm{d}K}{\mathrm{d}t} = \underbrace{-S\overline{uw}}_{=P} - \varepsilon - \sigma \sum \frac{\mathrm{d}S_b}{\mathrm{d}t} \tag{4.6}$$

where ε is the dissipation rate of turbulent energy and S_b the area of the bubble surface. The first and third terms in the right-hand side of Eq.4.6 represents the production rate of turbulent energy P and the temporal change of the surface energy, respectively. P is given by the product of the constant shear rate S and the Reynolds shear stress $-\overline{uw}$. Initially, the correlation between u and w is almost zero so that P is smaller than ε. The initial decay of K is caused by larger ε. On the other hand, as the flow evolves, P likely becomes positive (i.e., $-\overline{uw} > 0$) because the axial direction of the turbulent eddy which enhances its vorticity magnitude due to the mean shear is not homogeneous and such a selective enhancement of vorticity makes negative correlation between u and w. In the fully developed state, P becomes larger than other two terms, thus K increases monotonously. The growth of P is exponential and almost proportional to K. The effect of the bubble on the turbulence production is estimated by using P/K.

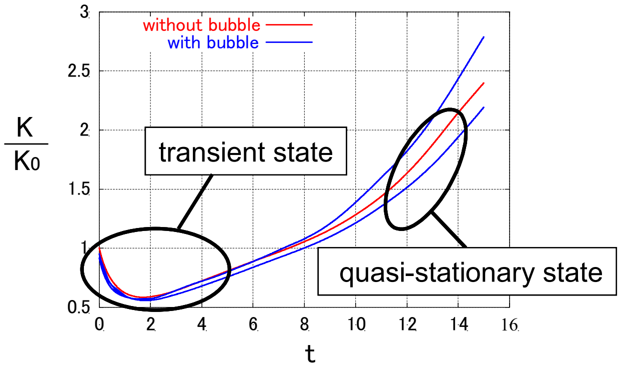

Fig. 4.4 Time change of turbulent energy

In order to determine the simulation condition, the parameters in the previous experiments performed by Moriguchi and Kato (2002) and Oishi *et al.*(2003) are referred as shown in Fig.4.5. The condition of the DNS is summarized in Table 4.1.

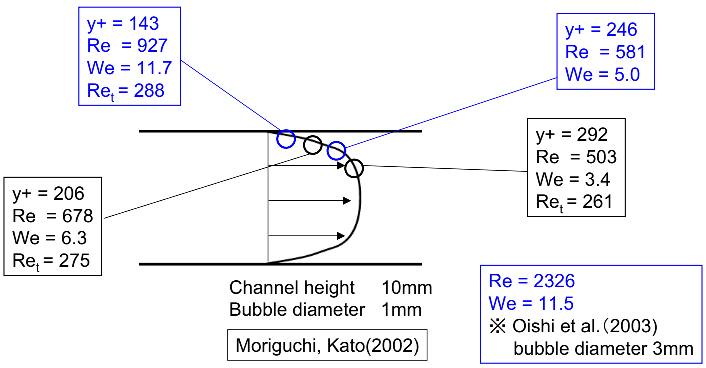

Fig. 4.5 Parameter of experiments

Table 4.1 Condition of DNS

Computational domain	1×1×1
Grid number	64^3 or 128^3
Bubble diameter	0.2, 0.133, 0.1
Shear Re number	2326, 1033, 927, 581, 258, 145
We number	11.5, 5.0
Turbulent Re number	20–350
d/l	0.2–0.9
Void ratio	3.35%

4.3 Computed results

The simulations were performed for different shear Reynolds numbers and initial turbulent Reynolds numbers, and the changes of the production P and the dissipation ε with respect to the values in the single phase flow are discussed.

The scaled production rates of turbulence energy P/K are shown in Figs. 4.6(a),(b) for different Reynolds numbers. The horizontal axis corresponds to the turbulent Reynolds number Re_t in order to make equitable comparison under the same turbulent intensity u_{rms}. Note that Re_t is proportional to $K^{1/2}$ so that it also grow exponentially in time in the fully developed state. As shown in the figures, the turbulent production P/K increase by adding the bubbles at the lower Reynolds number (Re=581). On the other hand, P/K reduces at the higher Reynolds number (Re=2326). This contradictory character of bubbles to increase or reduce the turbulence production is also observed as the increase or reduction of the skin friction in the channel flow in the previous experiments and numerical simulations (e.g., Murai *et al.*, 2004; Sugiyama *et al.*,2004). Moreover, the effect of the Reynolds number on the turbulence production is consistent with the previous studies.

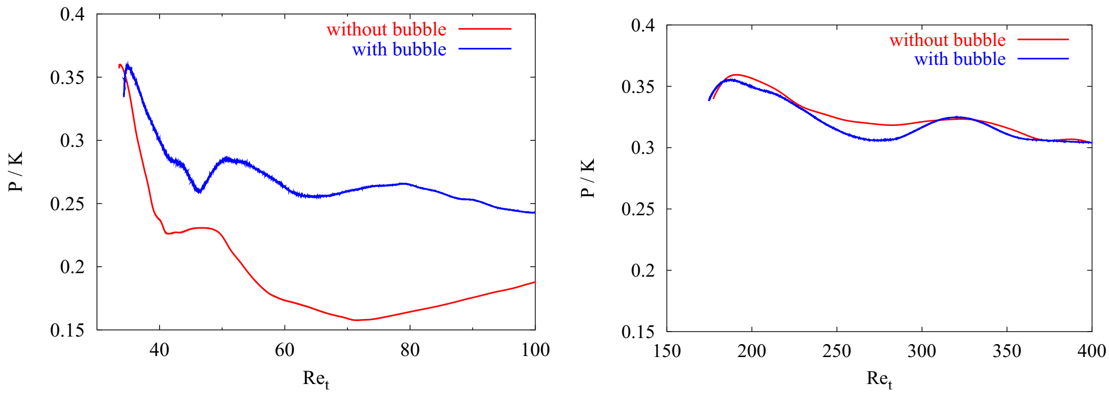

(a) Re=581 (b) Re=2326

Fig. 4.6 Normalized production of turbulent kinetic energy in the homogeneous shear flow

Figures 4.7(a), (b) show the normalized dissipation of the turbulent kinetic energy at Re=581, and Re=2326 respectively. Unlike the production, the dissipation increases by adding bubbles in both cases, but the changes are smaller than in the production. As a result the growth rate of the turbulent kinetic energy is increased at Re=581 and decreased at Re=2326. The decrease of the growth rate can be translated to the reduction of the frictional drag in the channel flow.

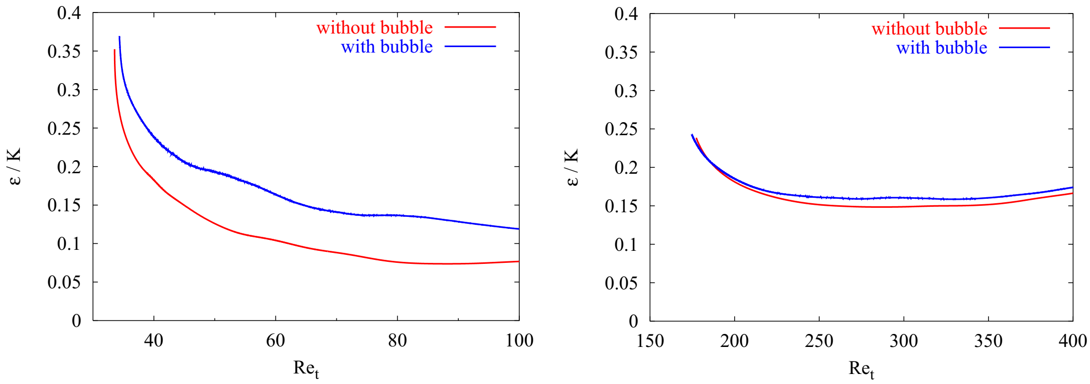

(a) Re=581 (b) Re=2326

Fig. 4.7 Normalized dissipation of turbulent kinetic energy in the homogeneous shear flow

In order to clarify both the mechanisms of the drag reduction and increase, the local flow modulation is examined by visualizing the structure of eddies. The vortical structure is educed by using the second invariant of the velocity gradient tensor Q (Hunt *et al*., 1988; Tanahashi *et al*.,1997). Q is given by,

$$Q = \frac{1}{2}\left(W_{ij} W_{ij} - S_{ij} S_{ij}\right),$$
$$S_{ij} = \frac{1}{2}\left(\frac{\partial u_i}{\partial xj} + \frac{\partial u_j}{\partial xi}\right), \qquad . \quad (4.7)$$
$$W_{ij} = \frac{1}{2}\left(\frac{\partial u_i}{\partial x_j} - \frac{\partial u_j}{\partial x_i}\right)$$

If Q is positive, $|W_{ij}|>|S_{ij}|$ i.e., the swirling motion exceeds the straing motion. According to Tanahashi *et al*.(1997), the indicator Q can be scaled by Kolmogorov length scale η and v_{rms} except for cases with considerably large Reynolds number. The scaled Q (written as Q^*) is given by,

$$Q^* = \frac{Q}{\left(v_{rms} / \eta\right)^2} . \qquad (4.8)$$

In the present study, the eddy is visualized with the isosurface of Q^*=0.05.

The vortex structures visualized by contour surfaces of the second invariant of the velocity gradient tensor (Jeong & Hussein, 1995) shown in Figures 4.8 and 4.9 indicate the different situations at Re=581 and Re=2326. At Re=581, in which bubbles increased the growth rate of the turbulent kinetic energy, strong organized vortices are formed in the wake of bubbles, while such structure is not present at Re=2326, in which bubbles decreased the growth rate. From the observation of the vortex structure at Re=581, the increase of the production by bubbles is supposed to be caused by the interaction between the bubbles and the mean velocity gradient. On the other hand, the figure for Re=2326 show that vortex structures are finer and rather independent of bubbles. In this case, the decrease in the production of turbulent kinetic energy is probably explained by the decreased freedom for turbulent structures to spatially develop.

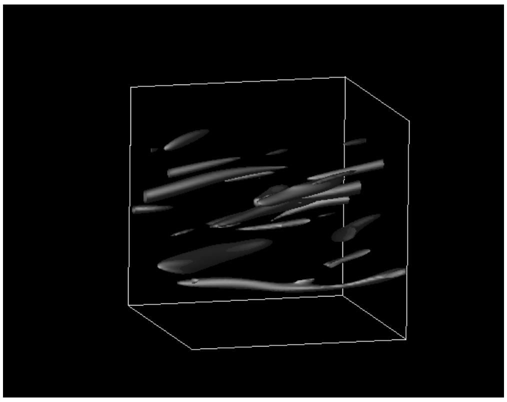

(a) Without bubbles.

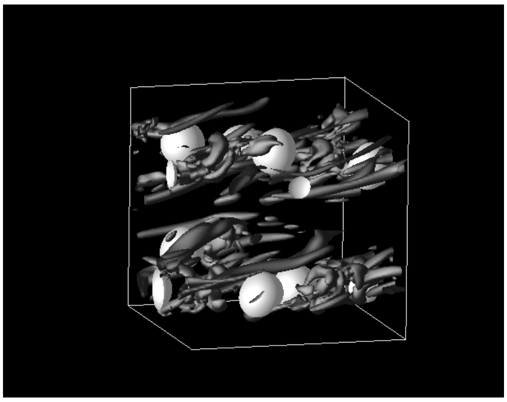

(b) With eight bubbles (α=3.35%)

Fig. 4.8 Vortex structures at Re=581

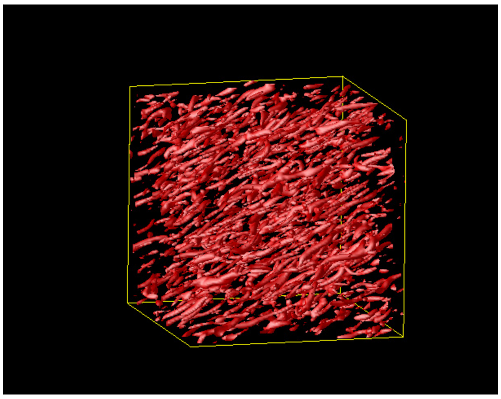

(a) Without bubbles

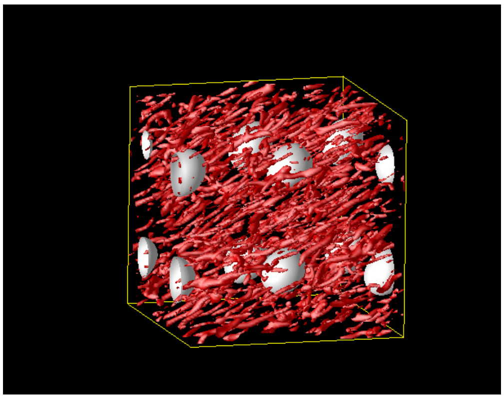

(b) With eight bubbles (α=3.35%)

Fig.4.9 Vortex structures at Re=2326

From the dimensional analysis and an assumption that the drag coefficient is in inverse proportion to the shear Reynolds number, the production added by bubbles is estimated to be proportional to

$$P_b = \frac{1}{\mathrm{Re}} \frac{\rho (Sd)^2}{d} \times (Sd) \tag{4.9}$$

For bubbles to decrease the production, this added production must be much smaller than the underlying production $P = -S\overline{uw}$, thus a new index, which determines whether bubbles increase or decrease the production, can be defined by P/P_b. By using u_{rms}^2 in place of $-\overline{uw}$, the following relation is derived.

$$P/P_b \propto \mathrm{Re}_t^2/\mathrm{Re} \tag{4.10}$$

By taking the square root of Eq (4.10), a new parameter is define as follows.

$$R = \mathrm{Re}_t/\sqrt{\mathrm{Re}} \tag{4.11}$$

The parameter R is the indication of the turbulent intensity relative to the mean velocity gradient.

Figure 4.10(a) shows the change of the production by bubbles versus the turbulent Reynolds number Re_t. It is noted that bubbles decrease the production as Re_t is increased, and that increase of the shear Reynolds number increases the production rate. Figure 4.10(b) shows the same value versus the new parameter R. Compared with Figure 4.10(a), a better correlation is confirmed. The change of the growth rate in Fig. 4.11 shows the negative values of the growth rate change, which is translated to drag reduction in channel flow, are observed when R is large.

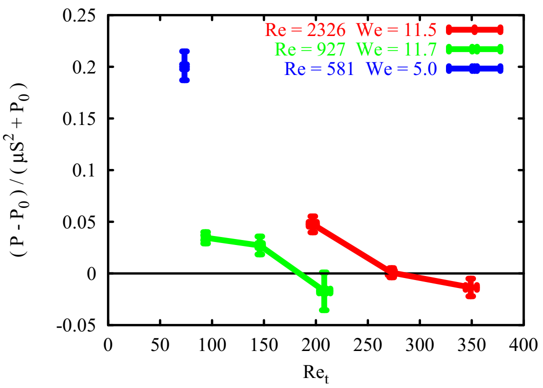

(a) Turbulent Reynolds number Re_t

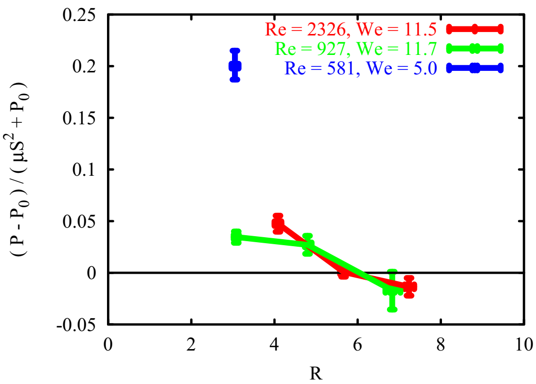

(b)Parameter $R = \mathrm{Re}_t/\sqrt{\mathrm{Re}}$

Fig. 4.10 The change of the production of turbulent kinetic energy by bubbles versus two parameters

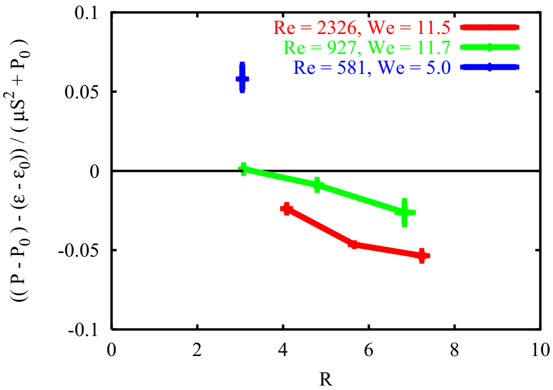

Fig. 4.11 The change of the growth rate of turbulent kinetic energy by bubbles versus the parameter $R = \mathrm{Re}_t / \sqrt{\mathrm{Re}}$

The hypothesis about the parameter R can also explain the different tendencies found in the simulation of channel flow at Re_t=180 and Re_t=1100. As shown in Fig. 4.12, the value of the R parameter is a factor of 2 larger at Re_t=1100 than at Re_t=180. Moreover, R does not depend on the bubble diameter. This is important to be consistent with the experimental evidence that the bubble diameter is not important.

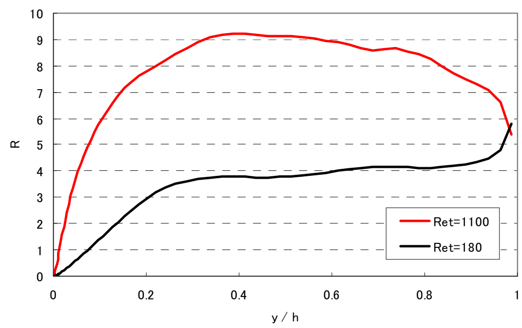

Fig. 4.12 Profiles of the parameter R at Re_t=180 and Re_t=1100

4.4 Summary of Chapter 4

From the simulation of the homogeneous turbulent shear flow, following results are obtained:

- Bubbles can either increase or reduce turbulence production depending on conditions.
- The important parameters are the shear Reynolds number, the turbulent Reynolds number and the Weber number.
- Large turbulent Reynolds number, smaller shear Reynolds number and large Weber number have positive influence on the microbubble drag reduction by bubbles.

5. Coclusions

As stated in the introduction, the main purpose of the present study is to carry out both experiment and numerical simulation of turbulent channel flows with bubbles at the same Reynolds number range and to compare the two results directly. Therefore Silicone oil was used as a fluid medium in the experiment in order to lower the Reynolds number to the range corresponding to DNS. The results of the experiment are shown in Section 2.3. In the DNS, two methods were used. One is FCM (Force Coupling Method), in which bubbles are regarded as rigid spheres, and the other is FTM (Front-Tracking Method), in which bubbles are deformable and therefore should be compared with experiments. The numerical results using FCM should be utilized to see the effect of bubble deformation. The FCM results are shown in Section 3.2, especially Section 3.2.4(2), and the FTM results are shown in Section 3.3.3.

The experimental conditions are shown in Tables 2.5 and 2.6 (U=1.51m/s or 2.03m/s). The computational conditions for FTM are shown in Table 3.5. The largest difference in the conditions is the Weber number *We*, which is approximately 200 for large bubbles in the experiment and 100 in the computation because of the limitation of numerical stability. In addition to the difference in the Weber number, the polynomial representation of bubble shape (Fig.3.17) prevents high deformation. Therefore we should expect that the bubbles in the computation are less deformed than those in the experiment, and by comparing Fig. 2.23 (U=1.5m/s) and Fig. 3.22(b) we see that this expectation is satisfied.

The Reynolds number of the experiment is either 2,777 at U=1.51m/s or 3,734 (or 3,811) at U=2.03m/s. The experimental values of local skin friction are shown in Figs. 2.21(a), (b). The two figures show that, although a trip wire is used for turbulent stimulation, the flow is semi-laminar at *Re*=2,777 in the non-bubble condition, and that, by injecting bubbles, the skin friction increases to the turbulent flow value, which means that bubble injection changes the flow to fully turbulent. Thus the result at *Re*=2,777 means that adding bubbles stimulates turbulence and results in skin friction increase. At *Re*=3,734(3,811) the flow is already fully turbulent in the non-bubble condition, and therefore adding bubbles has little influence on the flow, resulting in little change in the skin friction. At even higher Reynolds number of nearly 4,500 (see Fig. 2.21(b)), adding bubbles decreases skin friction slightly.

The Reynolds number of the numerical simulation using FTM is 3,000. The time history of skin friction is shown in Fig.3.20(a) and (b). At the wall where bubbles are clustered by buoyancy, local skin friction tends to show slight decrease by adding deformable bubbles. However, by adding less deformable bubbles local skin friction slightly increases. The local skin friction in the FCM computation at *Re*=4,000 shows 2.3% increase by adding bubbles, which are rigid (Fig.3.12). Therefore it may be stated that, at Re=3,000, addition of deformable bubbles tends to decrease skin friction, while addition of less deformable bubbles, or rigid bubbles, tends to increase skin friction.

Very recently, Lu et al.(2005) simulated the minimum channel flow with deformable bubbles using the Front-Tracking method and investigated the bubble deformation effect for various Weber numbers. They found that the spherical bubbles enhance the skin friction, while the highly deformed bubbles attenuate the strength of the streamwise turbulence vortices and consequently reduce the skin friction. Their finding agrees with ours.

The simulation of the homogeneous turbulent shear flow (HTSF) with deformable bubbles shows that large turbulent Reynolds number and large Weber number have positive influence on the microbubble drag reduction by bubbles. The increase of the turbulent Reynolds number of HTSF corresponds to the increase of the Reynolds number of the turbulent channel flow (TCF), and therefore the result agrees with the experimental result that added bubbles decrease skin friction at higher Reynolds number but not at lower Reynolds number. The Weber number dependence of the HTSF result can be compared directly with that of TCF. Thus the result confirms that bubble deformation acts to decrease skin friction.

Although the purpose of the present study is to compare directly experiment and numerical simulation of the turbulent channel flow with bubbles, the comparison has turned out to be not straightforward for two reasons. One reason is that in the experiment the flow is not fully turbulent and adding bubbles triggers turbulence at Re=3,000 or smaller. The other reason is that in DNS bubble deformation is limited due to the limitation in numerical stability. Further study is needed both experimentally and numerically in this respect. Use of silicone oil gives possibility of experiments in a parameter range significantly different from that using water, thus can help the elucidation of the skin friction reduction mechanism of microbubbles. Numerical simulation techniques of turbulent flow with deformable bubbles should be further improved. Especially high deformation and breakup of bubbles should be simulated.

Acknowledgment

This study was carried out as the NICOP program N00014-03-1-0299 sponsored by the Office of Naval Research. The authors would like thank Drs. Hitoshi Narita and Patrick Purtell of O.N.R. for their guidance in the course of the study.

References

Adrian, R.J. and Moin, P., 1988, Stochastic estimation of organized turbulent structure: homogeneous shear flow, *J. Fluid Mech.*, **190**, 531-559.

Ferrante, A., Elghobashi, S., 2004, On the physical mechanisms of drag reduction in a spatially developing turbulent boundary layer laden with microbubbles, J. Fluid Mech., 503, pp.345-355

Fukagata, K., Iwamoto, K., Kasagi, N., 2002, Contribution of Reynolds stress distribution to the skin friction in wall-bounded flows, Phys. Fluids, 14, pp.73-76

Fukuda, K., Tokunaga, J., Nobunaga, T., Nakatani, T., Iwasaki, T., 2000, Frictional drag reduction with air lubricant over a super-water-repellent surface, J. Marine Sci. Tech., 5, pp.123-130.

Gabillet, C., Colin, C., Fabre, J., 2002, Experimental study of bubble injection in a turbulent boundary layer, Int. J. Multiphase Flow, 28, pp.553-578

Gerz, T., Schumann, U. and Elghobashi, S.E., 1989, Direct simulation of stably stratified homogeneous turbulent shear flows, *J. Fluid Mech.*, **200**, 563-594.

Hassan, Y.A., 2004, Drag reduction by microbubble injection, Proc. 3rd Int. Symp. On Two-phase Flow Modelling and Exp., Pisa, pp.1-6

Hunt, J.C.R., Wray, A.A. and Moin, P., (1988) Eddies, stream and convergence zones in turbulent flows, Center for Turbulent Research Report CTR-S8.

Iwamoto, K., Suzuki, Y., and Kasagi, N., 2002., "Reynolds Number Effect on Wall Turbulence: Toward Effective Feedback Control," Int. J. Heat and Fluid Flow, Vol. 23, pp. 678-689.

Jeong, J. and Hussain, F., 1995, On the identification of a vortex, J. Fluid Mech., Vol.285, 69-94

Kataoka,I., Serizawa,A. 1898, Basic Equations of Turbulence in Gas-Liquid Two-Phase Flow, International Journal Multiphase Flow, 15, 5, pp.843-855.

Kato, H., Iwashina, T., Minyanaga, M., Yamaguchi, H., 1999, Effect of microbubbles on the structure of turbulence in a turbulent boundary layer, J. Mar. Sci. Tech., 4, pp.155-162

Katsui, T., Okamoto, Y., Kasahara, Y., Shimoyama, N., Iwasaki, Y., Soejima, S., Hirayama, A., 2003, A study of air lubrication method to reduce frictional resistance of ship, J. Kansai Soc. N.A., Japan, 239, pp.45-53 (in Japanese)

Kawamura, T. and Kodama, Y., 2001, Direct numerical simulation of wall turbulence with bubbles, Proc. of 2nd Symp. on Smart Control of Turbulence, The Univ. of Tokyo, Tokyo, Japan, 135-143.

Kawamura, T. and Kodama, Y., 2002, Numerical simulation method to resolve interactions between bubbles and turbulence, Int. J. Heat and Fluid Flow, 23, 627-638.

Kida, A. and Tanaka, M., 1992, Reynolds stress and vortical structure in a uniformly sheared turbulence, *J. Phys. Soc. Japan*, **61**, 4400-4417.

Kitagawa, A., Hishida, K. and Kodama, Y., 2004, Two-phase turbulence structure in a microbubble channel flow, *Proc. of the 5th Symp. on Smart Control of Turbulence,* 135-144.

Kodama, Y., Kakugawa, A., Takahashi, T., Kawashima, H., 2000, Experimental study on microbubbles and their applicability to ships for skin friction reduction, Int. J. Heat and Fluid Flow, 21, pp.582-588

Kitagawa,A., Hishida,K., Kodama,Y. 2004, Turbulence structures of microbubble flow measured by PTV/LIF/SIT, 5th International Conference on Multiphase Flow, CD-ROM, No.521, pp.1-12.

Kitagawa, A., Fujiwara, A., Hishida, K., Kakugawa, A., Kodama, Y., 2003, Turbulence structures of microbubble flow measured by PIV/PTV and LIF techniques, Proc. 4th Symp. on Smart Control of Turbulence, pp.131-140

Latorre, R., Miller, A., Philips, R., 2003, Micro-bubble resistance reduction on a model SES catamaran, Ocean Eng., 30, pp.2297-2309

Legner H.H., 1984, Simple model for gas bubble drag reduction, Phys. Fluids, 27, pp.2788-2790

Lee, M.J., Kim, J. and Moin, P., 1990, Structure of turbulence at high shear rate, *J. Fluid Mech.*, **216**, 561-583.

Lu, J., Fernandez, A. and Tryggvason, G., 2005, The effect of bubbles on the wall drag in a turbulent channel flow, Phys. Fluids, Vol.17, 095102.

Lomholt, S, Stenum, B. and Maxey, M.R., (2002) Experimental verification of the force coupling method for particlate flows, *Int. J. Multiphase Flow*, **28**, 225-246.

Madavan N.K., Deutsch S., Merkle, C.L., 1985, Measurement of local skin friction in a microbubble modified turbulent boundary layer, J. Fluid Mech., 156, pp.237-256

Marie, J.L., 1987, A simple analytical formulation for microbubble drag reduction, J. Phys-Chem Hydro. 13, pp.213-220

Matsumura, K., Kaminaga, F., Saito, H., 2002, Drag reduction on super water repellent surface with air injection method (2nd Report, Drag reduction mechanism)(in Japanese), Transactions JSME Series B, 68, 671, pp.32-38.

Maxey, M.R., Riley, J., 1983, Equation of motion for a small rigid sphere in a turbulent fluid flow, Phys. Fluids, 26, pp.883-889

Maxey, M.R. and Patel, B.K. 2001, Localized force representations for particles sedimenting in Stokes flow, *Int. J. Multiphase Flow*, **27**, 1603-1626.

McCormick, M., Bhattacharyya, R., 1973, Drag reduction of a submersible hull by electrolysis, Nav. Engg. J., 85, pp.11-11

Merkle, C.L., Deutsch S., 1992, Microbubble drag reduction in liquid turbulent boundary layers, ASME Appl. Mech. Rev., 45, 3, pp.103-127

Moriguchi, Y. and Kato, H., 2002, Influence of microbubble diameter and distribution on frictional resistance reduction, *J. Mar. Sci. Technol.*, **7**, 79-85.

Oishi, Y., Murai, Y., Ishikawa, M. and Yamamoto, F., 2003, PTV measurement of near-wall bubbly flow in a horizontal channel, *Proc. of Fluid Engineering Conference 2003, Japan Society of Mechanical Engineers*, 1302(CD-ROM).

Rogers, M.M. and Moin, P., 1987, The structure of the vorticity field in homogeneous turbulent flows, *J. Fluid Mech.,* **176**, 33-66.

Serizawa, A., Kataoka, I., 1990, Turbulence suppression in bubbly two-phase flow, Nucl. Eng. Des., 122, pp.1-16

Sugiyama, K., Kawamura, T., Takagi, S. and Matsumoto, Y., 2002, Numerical simulation on drag reduction mechanism by microbubbles, Proc. of 3rd Symp. on Smart Control of Turbulence, The Univ. of Tokyo, Tokyo, Japan, 129-138.

Sugiyama, K., Kawamura, T., Takagi, S. and Matsumoto, Y., 2003, Numerical simulation of transient microbubble flow, Proc. of 4th Symp. on Smart Control of Turbulence, The Univ. of Tokyo, Tokyo, Japan, 51-60.

Sugiyama, K., Kawamura, T., Takagi, S. and Matsumoto, Y., 2004, The Reynolds Number Effect on the Microbubble Drag Reduction, Proc. of 5th Symp. on Smart Control of Turbulence, The Univ. of Tokyo, Tokyo, Japan.

Tanahashi, M., Miyauchi, T. and Ikeda, J., 1997, Scalling law of coherent fine structure in homogeneous isotropic turbulence, *Proc. 11th Symp. on Turbulent Shear Flows*, **1**, 4-17.

Unverdi, S.O. and Tryggvason, G., 1992, A Front-tracking method for viscous, incompressible, multi-fluid flows, J. Comp. Phys., 100, 25-37.

Takahashi, T., Kakugawa, A., Makino, M., Kodama, Y., 2003, Experimental study on scale effect of drag reduction by microbubbles using very large flat plate ships, J. Kansai Soc. N. A., Japan, No.239, 2003, pp.11-20.

Xu, J., Maxey, M., Karniadakis, G., 2002, Numerical simulation of turbulent drag reduction using micro-bubbles, J. Fluid Mech., 468, pp.271-281